

A spectral data release for 104 Type II Supernovae from the Tsinghua Supernova Group

Han Lin,^{1,2,3,5} Xiaofeng Wang,^{1*} Jujia Zhang,^{3,4,5}† Shengyu Yan,¹ Danfeng Xiang,¹ Tianmeng Zhang,^{6,7,8} Xulin Zhao,⁹ Xinghan Zhang,¹⁰ Hanna Sai,¹ Liming Rui,¹ Jun Mo,¹ Gaobo Xi,¹ Fang Huang,¹¹ Xue Li,¹ Yongzhi Cai,^{1,3,4,5} Weili Lin,¹ Jie Lin,^{1,12} Chengyuan Wu,^{3,1} Jicheng Zhang,^{13,1} Zhihao Chen,¹ Zhitong Li,¹ Wenxiong Li,¹⁴ Linyi Li,¹ Kaicheng Zhang,¹ Cheng Miao,¹ Juncheng Chen,¹⁵ Zhou Fan,¹⁴ Jianning Fu,¹³ Shengbang Qian,¹⁶ Hong Wu,¹⁷ Xue-Bing Wu,¹⁸ Jingzhi Yan,¹⁹ Huawei Zhang,¹⁸ Junbo Zhang,¹⁷ Liyun Zhang,²⁰ Jie Zheng,¹⁴ Qian Zhai³

¹Physics Department, Tsinghua University, Beijing, 100084, China

²Key Laboratory of Radio Astronomy and Technology, Chinese Academy of Sciences, A20 Datun Road, Chaoyang District, Beijing, 100101, P. R.

³Yunnan Observatories, Chinese Academy of Sciences, Kunming 650011, China

⁴Key Laboratory for the Structure and Evolution of Celestial Objects, Chinese Academy of Sciences, Kunming 650011, China

⁵International Centre of Supernovae, Yunnan Key Laboratory, Kunming 650216, P. R. China

⁶Institute for Frontiers in Astronomy and Astrophysics, Beijing Normal University, Beijing, 102206, China

⁷Key Laboratory of Space Astronomy and Technology, National Astronomical Observatories, Chinese Academy of Sciences, 20A Datun Road, Beijing

⁸School of Astronomy and Space Science, University of Chinese Academy of Sciences, Beijing 101408, China

⁹School of Science, Tianjin University of Technology, Tianjin 300384, China

¹⁰School of Physics and Information Engineering, Jiangsu Second Normal University, Nanjing, Jiangsu 211200, PR China

¹¹Department of Astronomy, Shanghai Jiao Tong University, Shanghai 200240, China

¹²Department of Astronomy, University of Science and Technology, Hefei, China

¹³Department of Astronomy, Beijing Normal University, Beijing, 1000875, China

¹⁴Key Laboratory of Optical Astronomy, National Astronomical Observatories, Chinese Academy of Sciences, Beijing 100101, China

¹⁵Wuzhou University

¹⁶Department of Astronomy, School of Physics and Astronomy, Yunnan University, Kunming 650091, P. R. China

¹⁷National Astronomical Observatories, Chinese Academy of Sciences, Beijing 100101, China

¹⁸Department of Astronomy, School of Physics, Peking University, Beijing 100871, China

¹⁹Purple Mountain Observatory, Chinese Academy of Sciences, Nanjing, China

²⁰College of Physics, Guizhou University, Guiyang, China

Accepted XXX. Received YYY; in original form ZZZ

ABSTRACT

We present 206 unpublished optical spectra of 104 type II supernovae obtained by the Xinglong 2.16m telescope and Lijiang 2.4m telescope during the period from 2011 to 2018, spanning the phases from about 1 to 200 days after the SN explosion. The spectral line identifications, evolution of line velocities and pseudo equivalent widths, as well as correlations between some important spectral parameters are presented. Our sample displays a large range in expansion velocities. For instance, the Fe II 5169 velocities measured from spectra at $t \sim 50$ days after the explosion vary from 2000 km s^{-1} to 5500 km s^{-1} , with an average value of $3872 \pm 949 \text{ km s}^{-1}$. Power-law functions can be used to fit the velocity evolution, with the power-law exponent quantifying the velocity decline rate. We found an anticorrelation existing between $H\beta$ velocity at mid-plateau phase and its velocity decay exponent, SNe II with higher velocities tending to have smaller velocity decay rate. Moreover, we noticed that the velocity decay rate inferred from the Balmer lines (i.e., $H\alpha$ and $H\beta$) have moderate correlations with the ratio of absorption to emission for $H\alpha$ (a/e). In our sample, two objects show possibly flash-ionized features at early phases. Besides, we noticed that multiple high-velocity components may exist on the blue side of hydrogen lines of SN 2013ab, possibly suggesting that these features arise from complex line forming region. All our spectra can be found in [WiSeREP](#) and [Zenodo](#).

Key words: Techniques: spectroscopic – surveys – supernovae:general

* E-mail:wang_xf@mail.tsinghua.edu.cn

† E-mail:jujia@ynao.ac.cn

1 INTRODUCTION

Supernovae (SNe) with prominent hydrogen lines in their optical spectra are classified as type II supernovae (SNe II) (Minkowski 1941; Filippenko 1997). It is generally accepted that SNe II are produced by explosion of massive stars with initial masses $\geq 8M_{\odot}$ (Van Dyk et al. 2003; Smartt et al. 2009; Smartt 2009). The characteristic of SNe II display a wide variety in photometric and spectroscopic features. Based on the spectral and photometric features, SNe II can be divided into subclasses of SNe IIP, IIL, I Ib, and IIn etc. The subclasses of SNe IIP and IIL are primarily based on the shape of light curves. Those with almost constant luminosity (plateau) in light curves are called type IIP while those with a linear decline after maximum light are called type IIL (Barbon et al. 1979). Direct identifications of the progenitors of nearby SNe IIP, e.g. SN 2005cs (Maund et al. 2005; Li et al. 2006), SN 2012aw (Van Dyk et al. 2012; Fraser et al. 2012), SN 2017eaw (Kilpatrick & Foley 2018; Van Dyk et al. 2019; Rodríguez et al. 2020; Rui et al. 2019), et al. suggested that SNe IIP arise from red supergiant stars (RSG) with initial masses of 8-17 M_{\odot} . Among SNe IIP, some have low expansion velocities and less amount of nickel synthesized in the explosion, which are thought to represent the low luminosity tail of a continuous distribution in the parameter space of SNe IIP and probably originate from intermediate-mass (10 – 15 M_{\odot}) stars (Spiro et al. 2014; Zhang et al. 2014). Although SNe IIP and SNe IIL have different lightcurve shapes, there is increasing studies showing that no significant distinction exists between the observational properties of these two subclasses (Anderson et al. 2014; Sanders et al. 2015; Valenti et al. 2016; Galbany et al. 2016; de Jaeger et al. 2019). Anderson et al. (2014) found that more luminous SNe II tend to have faster post-peak declines and this trend could be used to estimate distances to SNe II (i.e., the photometric color method, de Jaeger et al. 2015). Gutiérrez et al. (2014) also suggested that there is no definitive spectral distinction between SNe IIP and SNe IIL. More luminous SNe II tend to have larger $H\alpha$ velocities and smaller ratios of absorption to emission (a/e) of $H\alpha$. Theoretical studies show that the plateaus in SNe IIP result from the combination of hydrogen envelope (Litvinova & Nadezhin 1983; Bartunov & Blinnikov 1992; Popov 1993; Morozova et al. 2015; Moriya et al. 2016), and the formation of SNe IIL can be due to that the exploding stars have less amount of hydrogen envelope (Anderson et al. 2014; Gutiérrez et al. 2017b).

Besides SNe IIP and SNe IIL, supernovae with long lasting narrow or/and intermediate-width emission lines of hydrogen in their optical spectra are classified as SNe IIn (Schlegel 1990). Different from ‘normal’ type IIP and type IIL SNe, circumstellar interaction (CSI) plays important roles in the observed properties of SNe IIn (Smith 2017). The spectra of some SNe II will evolve like SNe Ib a few weeks after the maximum light, which are called SNe I Ib and are thought to be the transitional objects linking between SNe II with stripped-envelope SNe Ib (Filippenko et al. 1993). An even more rare subclass of SNe II is 1987A-like events, which shows unusually long rise to the peak (Hamuy et al. 1988; Xiang et al. 2023). We do not include the subclasses of SNe IIn, SNe I Ib and 1987A-like events in this work.

With the wide-field, high-cadence transient surveys, the observed properties of both interesting individual objects and

large samples of SNe II have been studied. Spectroscopic observations provide important information on the physical origins and even stellar winds blown from their progenitors when the spectra can be obtained in very early phases. For example, the flash-ionized signatures allow constraints on the density and velocity of circumstellar material (CSM), and therefore the mass loss history shortly before the SN explosion (Gal-Yam et al. 2014; Shivvers et al. 2015; Khazov et al. 2016; Yaron et al. 2017; Lin et al. 2021; Zhang et al. 2023). On the other hand, the spectra in the nebular phase can be used to estimate the progenitor mass (Maguire et al. 2012; Jerkstrand et al. 2012; Silverman et al. 2017). In this paper, we present data and analysis of 206 spectra for 104 SNe II obtained by Tsinghua Supernovae Group during the period from 2011 to 2018. We describe our sample in Section 2. The spectral evolution and line identifications are presented in Section 3. The evolution of expansion velocities and the pseudo equivalent width (pEW) of some important spectral lines are presented in Sections 4 and 5, respectively. The correlations between these spectroscopic parameters are given in Section 6, and we conclude in Section 7.

2 DATA SAMPLE

Our sample consists of 206 unpublished spectra for 104 SNe IIP/L observed between 2011 and 2018. The spectra were obtained using the Xinglong 2.16-m telescope (+BFOSC/OMR; Fan et al. 2016) of NAOC and the Lijiang 2.4-m telescope (+YFOSC; Fan et al. 2015) of Yunnan Observatories. All the spectra were reduced using standard IRAF pipelines (Tody 1986, 1993), including bias and flat-field correction, cosmic-ray removal, wavelength and flux calibration. All spectra were corrected for atmospheric extinction using the extinction curves of the local observatories. Telluric absorptions were also removed for the spectra whenever possible.

For each SN, we used the same method following Gutiérrez et al. (2017a) to estimate their explosion dates. If high-cadence observations are available for the sample near the discovery, we adopt the midpoints between the last non-detection and the first discovery as the estimated explosion date. The lower and upper limits of the estimated explosion date will cover the non-detection and first-discovery epochs. For the object with sparse or without pre-discovery images, the explosion dates were estimated by matching spectral templates via the Supernova Identification (SNID) code (Blondin & Tonry 2007). SNID automatically gives matches that satisfy the default rlap cut ($rlap_{min} \geq 5$). In general, the best-fit templates are the first several templates that have the largest rlap values. The goodness of matching was also checked by eyes and we chose the best two from those rlap-ordered templates in most cases. The details of spectral matching and the plots with the best matches for each SN in our sample are shown in the supplementary materials. The explosion date is then taken as the average epoch of the two best-fit templates and the uncertainty is taken as the standard deviation of the average value. For those that the explosion dates can not be estimated from either the midpoint or the SNID fit, we have to treat the time of first discovery as the explosion

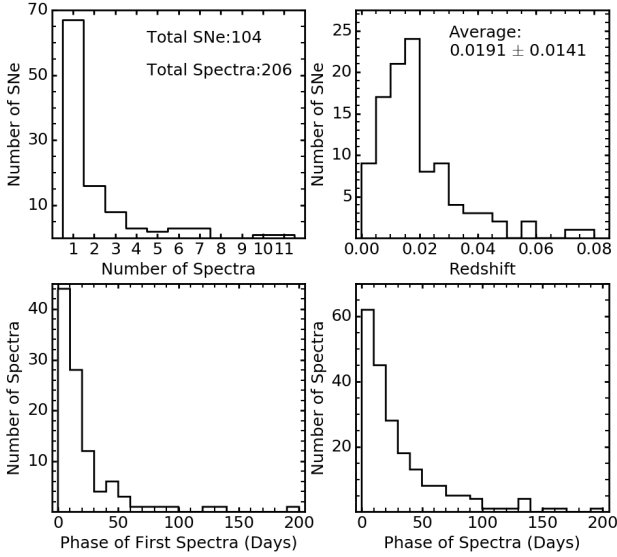


Figure 1. Distribution of SN-level and spectrum-level parameters. The upper-left panel shows the number of spectra per SN. The upper-right panel shows the redshift distribution of our sample. The lower-left and lower-right panels show the distribution of the phase of the first spectrum and all spectra, respectively.

dates¹. Among our 104 objects, 25 (24%) explosion epochs were obtained using midpoint, 35 (34%) were obtained using SNID template matching, while 25 (24%) have to use the time of first discovery as the estimated explosion time. It should be noted that some of our SN II samples have already been studied, and the explosion dates of this portion (about 18% of our sample) were taken from the literatures. The host galaxy redshifts of all our sample were taken from the NASA/IPAC extra galactic Database (NED) and the Galactic extinctions were from [Schlafly & Finkbeiner \(2011\)](#). The information of each SN II of our sample is listed in Table A1.

Figure 1 shows the statistical distribution of our sample, including the number of spectra, host-galaxy redshift, the phases of first spectrum and all spectra, respectively. A total of 206 spectra were collected for 104 objects. These spectra cover the phases from 1 days to 200 days after the explosion. Of the 104 SNe IIP/L, 37 objects have at least two spectra, while PS 15cwo has 11 spectra. A total of 20 objects (19%) were observed earlier than 5 days after the explosion and 46 object (44%) were observed earlier than 10 days after the explosion. The redshifts of these SNe II range from 0.00199 (SN 2012A) to 0.08 (SN 2017hcz), with a median value of 0.016, among which 78 objects (75%) are at hubble-flow distances ($z > 0.01$).

¹ Actually, for these objects, the time of first discovery is the upper limit of explosion date.

3 SPECTRAL EVOLUTION AND LINE IDENTIFICATION

3.1 Overall evolution of the spectra

The spectral evolution of our sample is shown in Figure A-1. The evolution of two well-observed SNe IIL (PS15cwo and SN 2018aoq), and the spectral line identifications are shown in Figure 2. One can see that the spectra at early phases are characterized by P-Cgyni profile of Balmer series and He I lines. The He I 5876 gradually evolves into Na I D absorption as the temperature decreases. For example, in the spectra of SN 2018aoq, the P-Cgyni profile near 5850 Å disappeared at $t \sim 20.5$ days after the explosion and it reappeared in the $t \sim 24.6$ day spectrum, with the new emergent feature being due to the Na I D absorption. As the SN ejecta expands and gets cooler, features from the inner materials start to appear in the spectra. For instance, at $t \sim 1$ month, the absorption feature of Fe II lines near 4800 Å to 4900 Å, including Fe II 5169, 5018, 4929, start to appear and get stronger with time. Later on, absorption features of other elements such as Sc II 6247, 5663, Ba II 6142, Ca II near-infrared (NIR) triplet and O I 7774 become visible in the spectra, and absorption features of Ba, Ti and Sc are blended with Fe II lines.

In the nebular phase, when the SN ejecta became transparent, the supernova is powered by the radioactive decay of ⁵⁶Co. At this late phase, the nebular spectra are dominated by emission lines due to recombination, collisional excitation and fluorescence ([Branch et al. 2001](#)). The prominent features include emission lines of H α , [O I] 6300, 6343, [Ca II] 7291, 7323 and Ca II NIR triplet (see Figure 3).

3.2 High velocity features of hydrogen

A few of SNe II are found to exhibit an extra absorption component on the blue side of H α lines. The notch could be the high velocity (HV) feature of H α or absorption of other species. [Gutiérrez et al. \(2017a\)](#) suggested that this absorption feature observed before $t \sim 35$ days after explosion can be associated with Si II 6355 line, while those observed after the middle of the plateau are HV features of hydrogen. There are two explanations proposed for the origin of the HV features. [Baron et al. \(2000\)](#) suggested that the blue side absorption can be due to the second P-Cgyni profile of H α caused by non-LTE effects. They reproduced the second absorption of H β line in their synthetic spectra with the full non-LTE atmosphere code PHOENIX. On the other hand, the HV features were also regarded as signs of interaction between SN ejecta and the CSM ([Chugai et al. 2007](#)), which can be used to estimate the mass loss rate of the progenitor star. In theory, the X-rays from the reverse shock can ionize and excite the outer layers of the ejecta, producing a shallow depression in the blue wings of absorption part of P-Cgyni profile ([Chugai et al. 2007](#)). Moreover, the HV features can also result from cold dense shell, and such an absorption is usually deeper ([Chugai et al. 2007](#)). Owing to the observed diversity of absorption shape, [Gutiérrez et al. \(2017a\)](#) suggested that these HV features are most likely produced by interaction.

For our sample presented in this work, we examined the blue part of H α in each spectrum and consider the notch as HV feature of H α if there is a similar absorption in H β

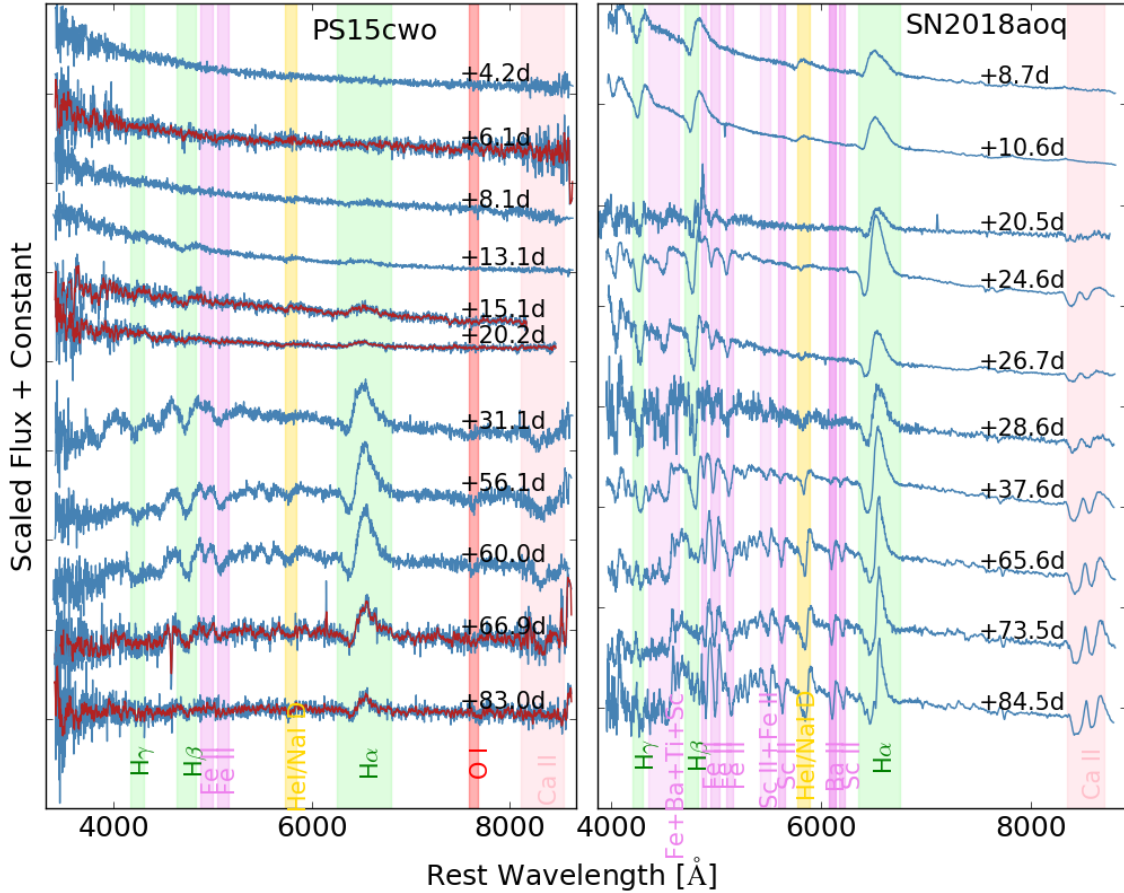


Figure 2. Spectral evolution and line identifications of PS 15cwo and SN 2018aoq. Shaded regions of different colors represent different spectral lines, with green representing hydrogen, yellow representing He I or Na I, purple representing iron, barium and other metal elements, respectively

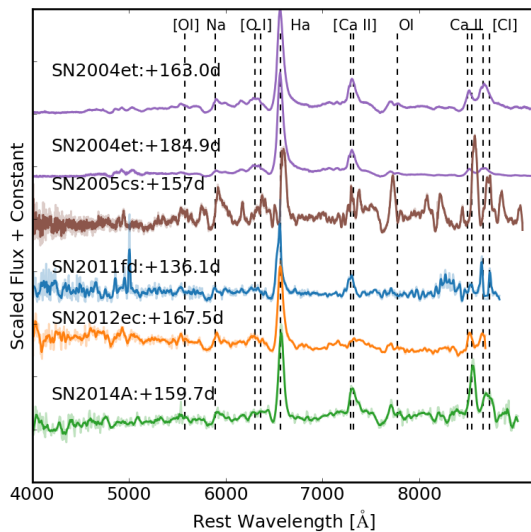


Figure 3. Nebular-phase spectra and line identifications for several SNe II objects in our sample.

line profile. The spectra with clear HV features are shown in Figure 4, where one can also see that these HV features show significant diversities. The notches seen in SN 2012A and SN 2016B are shallower, while those seen in SN 2012ec, SN 2012fs and SN 2018aoq are deeper. As CSM interaction can produce different shapes of HV features, we suggested that CSM interaction be more likely to produce the HV features.

We noticed that SN 2013ab likely showed two HV features in $t \sim 76$ day spectrum, with the absorption minima locating at 9000 km s^{-1} and 6500 km s^{-1} , respectively. We further examined its $t \sim 75$ day spectrum from [Silverman et al. \(2012\)](#) and found that the $H\beta$ did have two distinct absorptions, though the corresponding absorption in $H\alpha$ is very weak at 6500 km s^{-1} and we were not sure if this absorption really existed. Nevertheless, multiple notches are found to exist in other individuals. For instance, SN 2001X seems to have two notches detected in the same spectra (see Figure 18 in [Faran et al. 2014a](#)). However, [Faran et al. \(2014a\)](#) noticed that such an identification of HV feature is dubious as the velocities of $H\alpha$ and $H\beta$ do not match. Another sample is SN 2009N, where two absorption features next to $H\alpha$ (i.e., an absorption with a velocity of about 8000 km s^{-1} and another absorption with a lower velocity) were detected at the same time

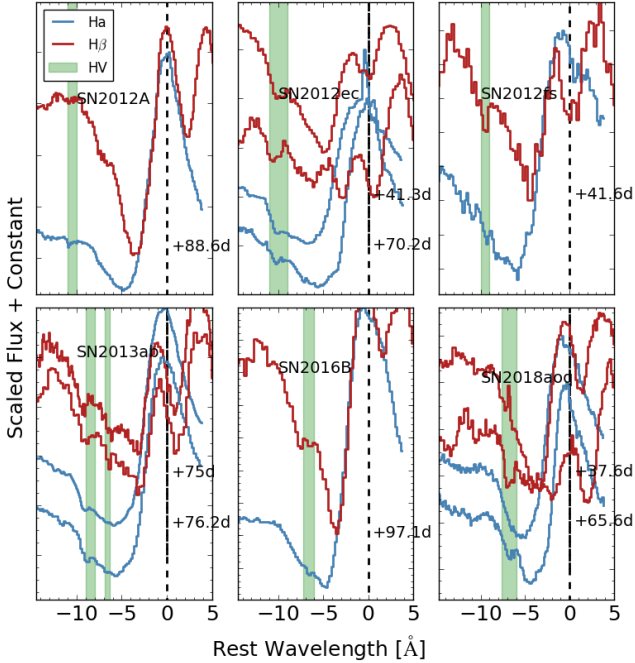


Figure 4. High Velocity features of hydrogen identified in our sample. Blue lines represent line profile of $H\alpha$ while red lines represent that of $H\beta$. The high velocity notches are marked by green shadow region. HV features have different shape: the notch of SN 2012A and SN 2016B are shallower, while SN 2012ec, SN 2012fs, SN 2018aoq are deeper. We found two notches in the $t \sim 76.2$ d spectrum of SN 2013ab at 76.2d, with the absorption minima locating at 9000 km s^{-1} and 6500 km s^{-1} , respectively. The overplotted $t \sim 75$ d spectrum of SN 2013ab is taken from [Silverman et al. \(2012\)](#).

in its spectra ranging from 62 days to 77 days after the explosion ([Takáts et al. 2014](#)) (see their Fig 9). In SN 2009ip, four notches are found to be embedded in the blue side of $H\alpha$ and its polarization spectra reveal a possibly clumpy line forming region. It is possible that some notches shown in the spectra of these objects belongs to other species instead of hydrogen. Otherwise, multiple HV features may indicate complex structure of line forming region which is possibly produced by interactions with asymmetric CSM.

3.3 Flashed-ionization Features

[Khazov et al. \(2016\)](#) estimated that $\geq 18\%$ of SNe II tend to show ionization emission lines (flash ionized, FI) in their spectra if they are observed at sufficiently early times. Such FI features are formed by the recombination of the outermost CSM, which has been ionized by high-energy photons created during SN shock breakout ([Gal-Yam et al. 2014](#)). In our sample, narrow $H\alpha$ emission is primarily used to identify the flash-ionized signatures as it is stronger and lasts for longer time. Ionization emission lines of other species, including helium, carbon, nitrogen and oxygen are also used whenever possible. As narrow emission lines of hydrogen can be easily contaminated by host-galaxy H II region, the objects with clear emission lines of host galaxy (e.g. [O III] 5007,

S II 6717, 6730) but without emission lines of other species except hydrogen, are not assigned as SN II sample with FI features (e.g. SN 2016hvu, see Figure A-1). Finally, we identified possible FI features in two objects, i.e., SN 2013ac and SN 2016aqw, among the 49 objects with spectra taken within 11 days after the explosion, (see Figure 5). The narrow emission lines of He I 5876, 7065 were observed in SN 2013ac and SN 2016aqw. In addition, the He II 4686 line (may blend with C III/N III) can be observed in the spectra of SN 2016aqw. Lorentzian function is used to measure the full width at half maximum (FWHM) of $H\alpha$ line profile, with the FWHM being $\sim 1000 \text{ km s}^{-1}$ and $\sim 800 \text{ km s}^{-1}$ for SN 2013ac and SN 2016aqw, respectively (see Figure A2). Note that for SN 2013fs, the FI feature can not be detected in our 5.4d spectrum, however, the emission features of O VI 3811, O V 5597, O IV 3410, N V 4604 and He II 4686 were detected in spectra that taken at earlier epochs than we observed ([Yaron et al. 2017](#)). Broad emission (with FWHM $\sim 5000 \text{ km s}^{-1}$) has been detected at the location of $H\alpha$ in SN 2016fmt. However, a narrow component seems to be superposed on the broad component (see Figure A2) and a possible emission signature of C IV 5801 seems to be detected, suggesting that SN 2016aqw possibly has FI features.

Besides the object with FI features, 19 of all 49 objects only show blue featureless spectra at early times (≤ 11 d). The phases of these spectra range from 1.1 days to 9.3 days after explosion. As the FI features usually disappear quickly, detection of such features require observations of SNe II within a few days after their explosions. SNe II with only blue featureless continuum probably produce no FI features at all or show FI signatures in the spectra at an epoch earlier than we observed.

4 EXPANSION VELOCITY

We measured the velocities of $H\alpha$, $H\beta$ and Fe II 5169 from the absorption minima of P Cgyni profiles in every spectrum where they can be clearly detected. At around the absorption minima, we choose a few regions with lower spectral flux density to measure the velocity. The average value of these measurements is used as the velocity and the standard derivation is used as the uncertainty. The results are shown in Figure 6 and tabulated in Table A3. For comparison, we also included the average velocity evolution from the sample of [Gutiérrez et al. \(2017a\)](#), the typical IIP SN 1999em ([Elmhamdi et al. 2003](#); [Takáts & Vinkó 2012](#)), the high-luminosity type IIP SN 2012aw ([Bose et al. 2013](#)) and the low-luminosity SN IIP 2005cs (LLSNe) ([Pastorello et al. 2009](#)). In Figure 6, we see that all of our SNe except for SN 2016cok have velocities larger than SN 2005cs, which means that SN 2016cok could be a low-luminosity SN II. [Kochanek et al. \(2017\)](#) identified a pre-explosion counterpart to SN 2016cok in archival images of Hubble Space Telescope and they found that the initial mass of progenitor was most likely in the mass range of $8 \sim 12 M_{\odot}$. Such a relative lower mass range is consistent with that expected for the progenitor stars of low-luminosity SNe.

As the SN ejecta expand homologously, thus the expansion velocities decrease with time approximately in a power-law fashion ([Faran et al. 2014a](#); [de Jaeger et al. 2019](#)). We thus fit the velocity evolution with a power-law function (i.e., $v_{H\alpha} = v_{H\alpha}^{50} (t/50)^{n_{H\alpha}}$, $v_{H\beta} = v_{H\beta}^{50} (t/50)^{n_{H\beta}}$, $v_{Fe} = v_{Fe}^{50} (t/50)^{n_{Fe}}$) to

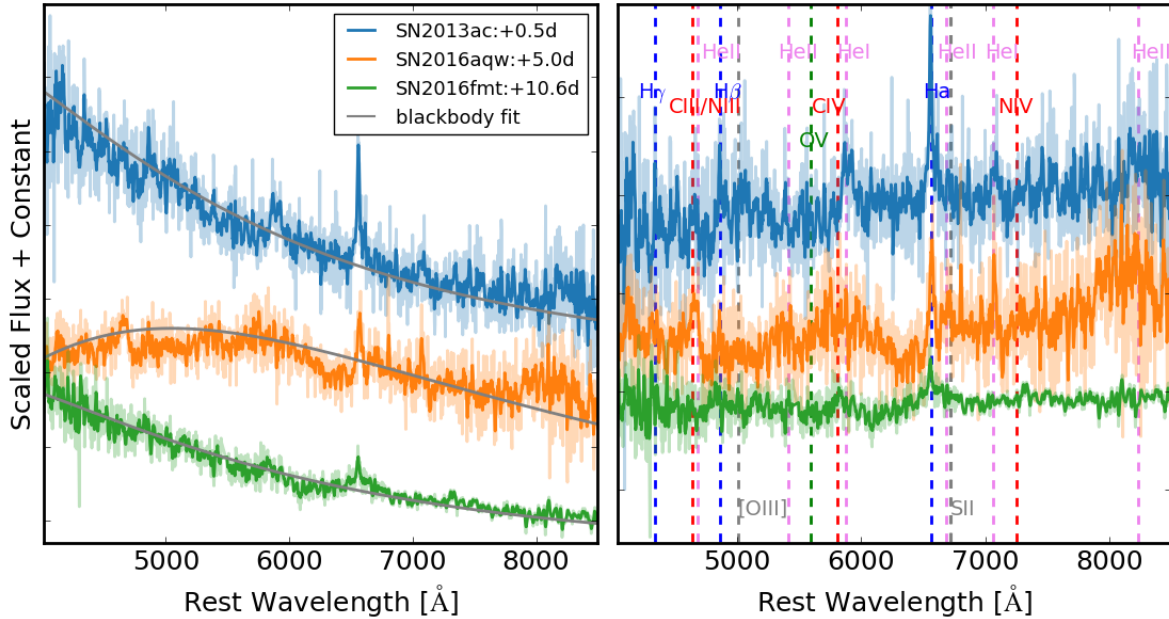


Figure 5. The SNe II of our sample showing possible flash ionized features in the early phases. Left panel: the original spectra and the best-fit blackbody (gray line). Right panel: the blackbody continuum-subtracted spectral features. Vertical dashed lines represent emission lines of different species.

estimate both the velocity at $t = 50$ days after the explosion and the power-law exponent. Power-law fitting can only be used for those having at least two velocity data points. In our sample, however, many SNe have only one spectrum. If their spectra were taken between 45 to 55 days after the explosion, the velocity measured by absorption minimum can be treated as v_{50} and they are included in our analysis to increase the number of statistics. The parameters of v_{50} and the power-law exponent are shown in Table A4. The velocity evolution of a part of SNe II and the fitting results are shown in Figure A3, and the distribution of these parameters are shown in Figure 7. At $t \sim 50$ days after the explosion, the velocities have large varieties. For instance, the velocity of $H\alpha$ ranges from 4500 to 10,000 km s^{-1} , with a mean value of $6904 \pm 1336 \text{ km s}^{-1}$, while the velocities of $H\beta$ range from 3000 to 10,000 km s^{-1} and the velocity of Fe II 5169 range from 2000 to 5500 km s^{-1} . As seen from Figure A3, for each SN, the velocity of hydrogen is higher than that of iron at similar epoch. This can be explained as that the Balmer lines are formed at larger radii than the iron lines.

Gutiérrez et al. (2017a) introduced $\Delta v(H\beta)$ (the mean velocity decline rate in a fixed phase range) to quantify the decline rate of $H\beta$ velocity. They found that SNe II with larger decline rates at early times continue to show such behaviors at late times. In our analysis, we use the power-law exponent (e.g., $n_{H\alpha}$, see Section 4) to describe the velocity decline rate. Larger absolute values suggest faster decline rates. As seen from Figure 7, the exponent measured from $H\alpha$ velocity evolution ranges from -0.45 to -0.15 and has a smaller range compared with those inferred from $H\beta$ and Fe II 5169 velocities. For example, the exponent inferred from the $H\beta$ velocity evolution has a range of -1.1 \sim -0.15. Among our sample, SN 2018bek, SN 2013gd and SN 2011az are the three showing the fastest decline rate of $H\beta$ velocity. The exponent

derived from Fe II 5169 velocity is found to vary from -1.1 to -0.2, with SN 2015V and SN 2016jfu are the two showing the fastest decline rates and SN 2011bi and PS15cwo showing the slowest decline rates. However, it should be pointed out that the power-law exponent was derived from only a few data points, which may suffer large uncertainties. Sometimes we may overestimate or underestimate the decline rate. For example, the $n_{H\beta}$ of SN 2013gd, n_{Fe} of SN 2015V and n_{Fe} of SN 2016jfu may be overestimated as shown in Figure A3.

5 PSEUDO-EQUIVALENT WIDTHS

The pseudo equivalent width (pEW) is used to describe the strength of spectral lines. We measured the pEW of the absorption part of $H\alpha$, $H\beta$ and Fe II 5169 lines, the emission part of $H\alpha$ and the pEW ratio of absorption to emission component (a/e) of $H\alpha$. The measurement results of our sample and the average values from sample presented in Gutiérrez et al. (2017a) are shown in Figure 8. One can see that the measurements of our sample are consistent with those derived by Gutiérrez et al. (2017a), although it is complicated to determine by the underlying continuum of each line feature.² The pEW of absorption component can reach at $\sim 100 \text{ \AA}$, $\sim 80 \text{ \AA}$, and $\sim 70 \text{ \AA}$ for $H\alpha$, $H\beta$ and Fe II 5169, respectively, while the emission component of $H\alpha$ can reach at $\sim 300 \text{ \AA}$ in the first ~ 140 days. As noted by de Jaeger et al. (2019) and Gutiérrez et al. (2017a), generally speaking, the absorption components of Balmer lines and Fe II lines tend to increase their strengths with time in the first one or two months and

² In our work, the continuum is determined by a linear fit to the two ends of the spectral line and the uncertainty of pEW is estimated by changing the range of two ends.

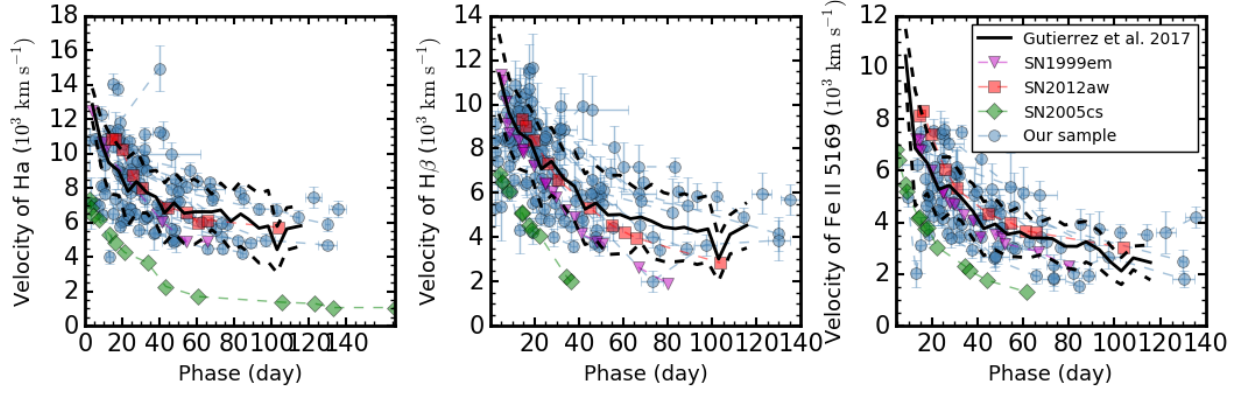


Figure 6. Velocity evolution of $H\alpha$, $H\beta$ and $Fe\ II\ 5169$ lines of our SN II sample and some well-studied SNe II. The blue circles represent our sample, while the black solid line and dashed lines represent the average velocity evolution and $1 - \sigma$ standard deviation from the sample of [Gutiérrez et al. \(2017a\)](#).

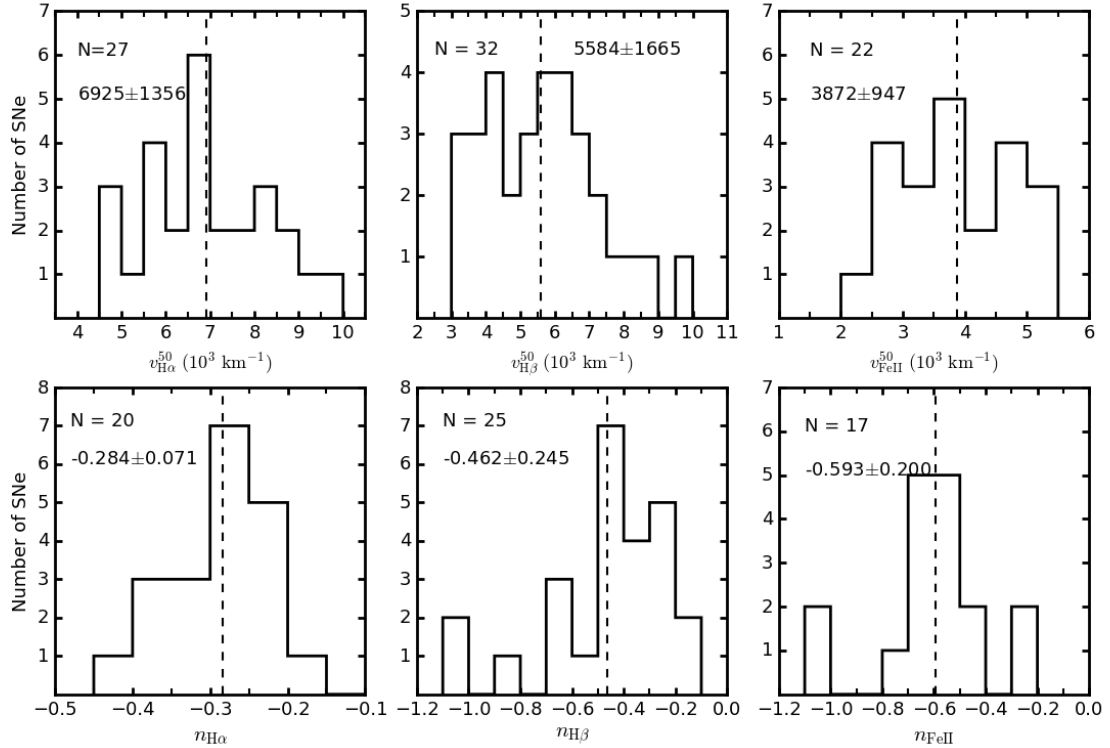


Figure 7. Distribution of velocity measured at $t \sim 50$ days after the explosion and the power-law exponents of $H\alpha$, $H\beta$ and $Fe\ II\ 5169$. The vertical dashed lines mark the average values. The total number and the average velocity (the unit of average velocity is $km\ s^{-1}$) of each parameter are listed in each panel.

this increase behavior becomes slowly at later phases. However, the pEW evolution shows diversities among different objects. For example, the absorption part of $H\alpha$ in PS15cwo, SN 2013gd and SN 2018aoq start to decrease in strength at $t \sim 60$ -70 days after explosion, while this happened in SN 2016cok since $t \sim 15$ days after the explosion. Diversities are also observed in the evolution of $H\alpha$ emission component. The evolution shows an overall increase with time but several objects show a decrease trend at some point. The general tendency of a/e shows an increasing tendency at early times and it remains constant or shows slight decrease at late times.

The large diversities in the strength of the above lines among different SNe II may reflect diverse temperature evolution and progenitor metallicity ([Gutiérrez et al. 2017a](#)).

6 PARAMETERS OF VELOCITY EVOLUTION

6.1 Correlations between velocity parameters

For these velocity parameters measured for our sample, we use the Pearson correlation coefficient (ρ) to examine their

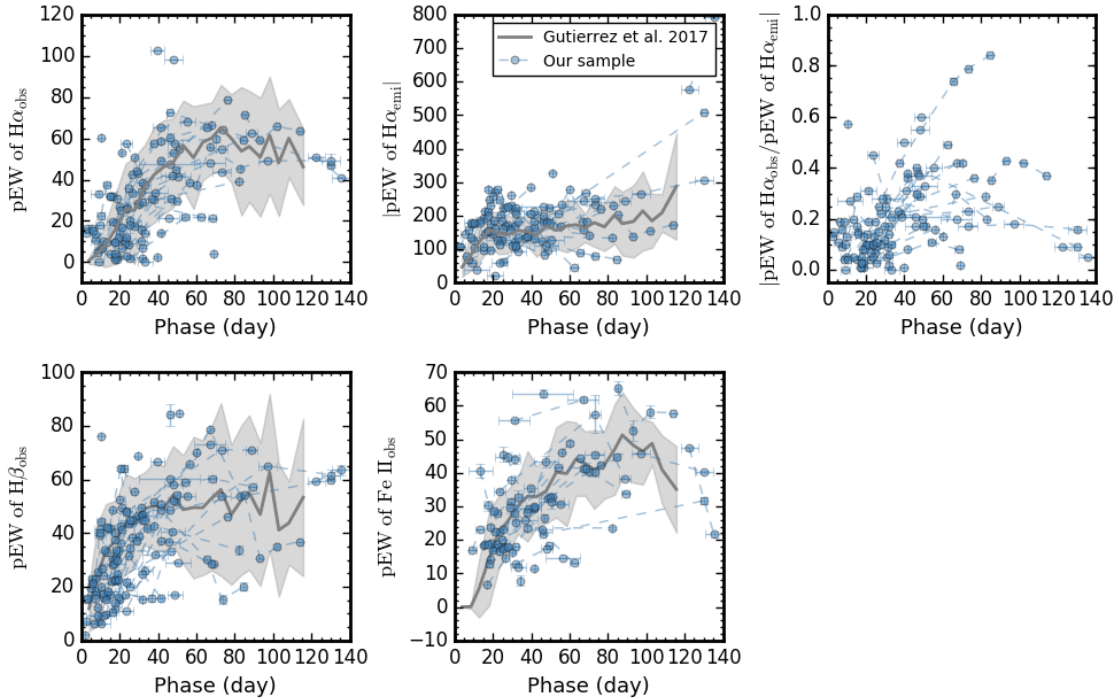


Figure 8. Temporal evolution of pEW of H α , H β and Fe II 5169. The blue dots and the gray shadow represent the average pEW value and 1σ standard deviation from the sample given by [Gutiérrez et al. \(2017a\)](#)

correlations. According to [Evans \(1996\)](#), the coefficients in the range of 0-0.19, 0.2-0.39, 0.4-0.59, 0.6-0.89 and 0.8-1.0 represent no, weak, moderate, strong, and very strong correlations, respectively. The results are shown in Figure 9. For the velocities measured at 50 days after the explosion, we found that any two of $v_{H\alpha}^{50}$, $v_{H\beta}^{50}$ and $v_{FeII5169}^{50}$ parameters show a strong positive correlation, with the Pearson correlation coefficient being larger than 0.8 (see the left three panels of Figure 9). However, for the evolution exponent $n_{H\alpha}$, $n_{H\beta}$ and n_{Fe} , we find no correlation between them, as shown in the middle panels of Figure 9. Besides, we found that the H β velocity tends to show a slower decline for SNe II with higher velocities. (see panel (f) of Figure 9). After excluding SN 2018bek, SN 2013gd and SN 2011az, which are the three showing the fastest velocity declines³, the Pearson coefficient increase from 0.586 to 0.660.

To test whether the above negative tendency really exists for SNe II, we further include some well-studied individual SNe II from the literature and those of [Gutiérrez et al. \(2017a\)](#) in the statistical sample. The velocity evolution and power-law fit for these well studied objects are shown in Figure A4 and the relevant parameters of these well-studied sample are also given in Table A4. The power-law fitting and the parameters for the sample of [Gutiérrez et al. \(2017a\)](#) are shown in Figure A5 and Table A5, respectively. For each spectral species, Pearson correlation coefficients were calculated for all the samples and for only the gold sample, respectively. (Those with error of power-law exponent less than 20% are

selected as the gold sample and they are represented by solid markers in Figure 10.) As can be seen from Figure 10, the tendency that high-velocity SNe II have slower velocity gradients still remains for H β when including more objects. Similar tendency probably exists in H α , with the Pearson coefficient being 0.45 for all sample and 0.65 for the well-observed SNe II from literature (after removing SN 2016bkv). [Faran et al. \(2014b\)](#) found that the velocities inferred from hydrogen lines of SNe IIL, especially H β , evolve more slowly than those of SNe IIP. In general, the velocities of SNe IIL are higher than those of SNe IIP, which means that SNe II with higher H β velocities also evolve more slowly in the samples of [Faran et al. \(2014b\)](#). Therefore, what they found is consistent with the negative correlation in H β revealed in this work. In comparison, the velocity decline rate of hydrogen derived in this work shows a continuous distribution and no distinction is found between the whole SNe II sample.

Besides, a negative correlation possibly exists in Fe II velocity and its velocity decay. However, we caution, that the negative correlation is not evident in the well-studied sample and the parameter distribution of Fe seems to have a larger scatter than that of hydrogen. Moreover, both [Faran et al. \(2014b\)](#) and [de Jaeger et al. \(2015\)](#) suggested that the Fe II velocity of SNe IIL shows a similar evolution as that of SNe IIP (but with a significant scatter), which is not consistent with the negative correlation. Therefore, we can not conclude the correlation between Fe II velocity and its decay rate.

As shown in Figure 10, the velocity parameters of some objects deviate from others. In some cases, the power-law results seem unreasonable due to bad spectral sampling (e.g., SN 2015V and SN 2016jfu). In other cases, the velocities evolve in distinct ways. The velocities of both SN 2016bkv (a low-

³ The point of SN 2017ivu is also removed since it is an outlier which probably due to bad spectral sampling.

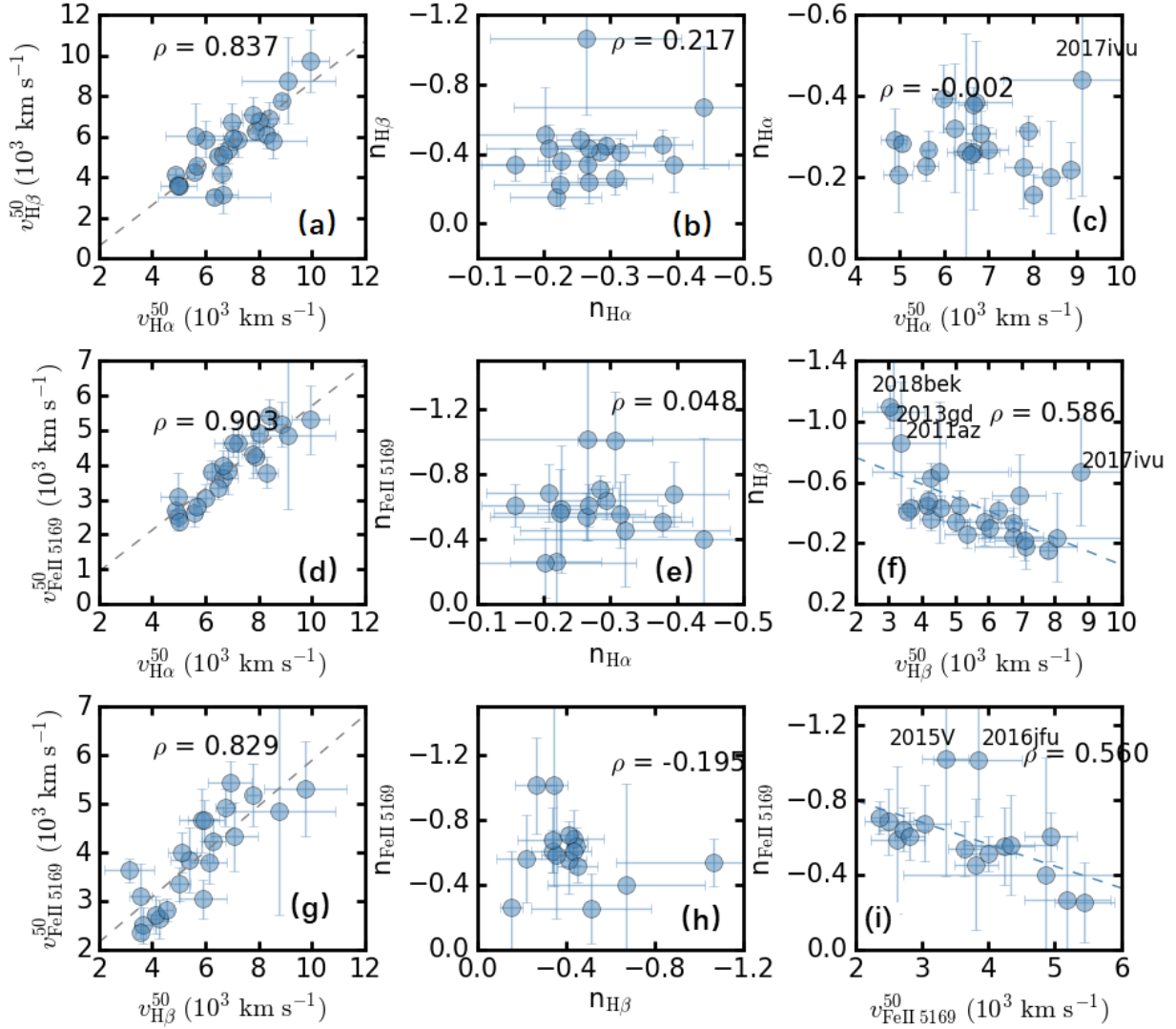


Figure 9. Correlations between velocity evolution parameters inferred from H α , H β , and Fe II 5169 lines. v^{50} represents the velocity derived from $t \sim 50$ d spectra, while $n_{H\alpha}$, $n_{H\beta}$ and n_{Fe} represents the power-law index determined by applying the power-law fits to the velocity decay from the H α , H β and Fe II 5169 absorption features, respectively.

luminosity SN II) and SN 2018zd show an increase at early times, which may be related to CSM interaction (Zhang et al. 2020), as shown in Figure A4. Moreover, the velocity parameters of SN 2016bvk seem to show significant differences from others. Nakaoka et al. (2018) also noticed that SN 2016bvk showed a slower velocity evolution when compared with other LL SNe. It is not clear why some LL SNe II deviate from the "normal" SN II sample in the $v^{50} - n$ relation. The evolution of velocity is related to the physical properties of the progenitor star and expansion itself. Since SN 2016bvk could be the possible electron-capture supernovae candidate (Hosseinzadeh et al. 2018), its distinct velocity evolution may be partly related with the possible electron-capture origin.

6.2 Correlations between pEW and velocity

The ratio of absorption part to emission part (a/e) of H α can be used to describe the diversity of SNe II. Patat et al. (1994)

and Schlegel (1996) proposed that the subclass of SNe IIL have shallower P-Cgyni profiles, and hence smaller a/e values. Whereas Gutiérrez et al. (2014) proposed that there is no definitive spectral distinction between SNe IIP and SNe IIL, and SNe II with smaller a/e ratios of H α tend to have higher H α velocities, more rapid post-peak declines in light curve, higher peak brightness, and shorter optically thick phase duration (defined as time from the explosion epoch through the end of the plateau phase.). Our spectral dataset also indicate that SNe II with higher H α velocities have smaller a/e ratios. Moreover, the exponents of velocity decay inferred from hydrogen lines seem to have a moderate correlation with the a/e values (see Figure 11), suggesting that the velocity evolution of hydrogen lines may be related to the hydrogen envelope. Faran et al. (2014b) proposed that the velocities of SNe IIL evolve more slowly than those of SNe IIP is due to that the hydrogen lines are formed in the outer thin layers of the ejecta rather than in a thick, gradually-exposed hy-

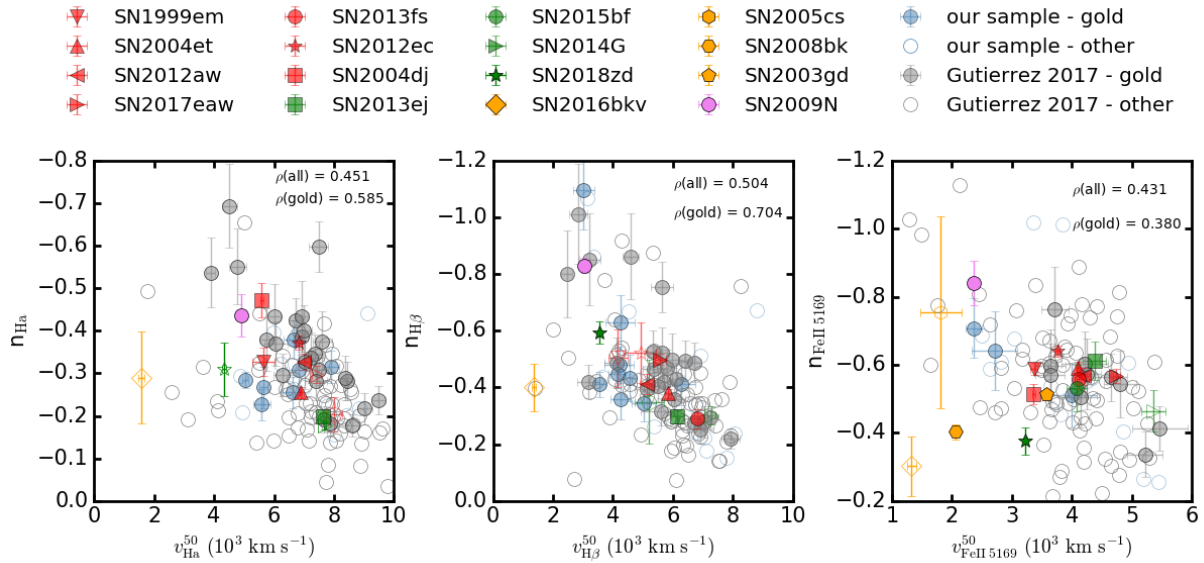


Figure 10. Similar as Fig 9, with well-studied individuals in literature included. Blue circles represent the data presented in this paper, while other well-studied sample are denoted by different symbols, with red symbols representing "typical" SNe IIP, green symbols representing fast-declining objects and yellow ones representing low-luminosity SNe II, respectively. The solid markers represent the gold sample which satisfies the criteria that the uncertainty is less than 20%, while the open markers represent other objects.

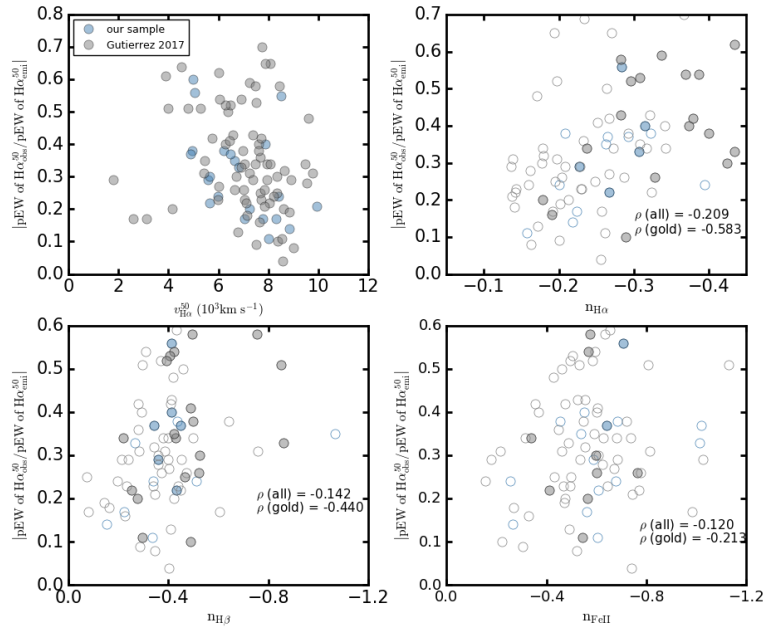


Figure 11. Correlation between pEW ratios of absorption to emission component (a/e) of $\text{H}\alpha$ and the velocity power-law exponents. In the upper-right, lower-left, and lower-right panels, the gold sample (The definition of a gold sample is the same as Figure 10) are represented by solid markers, while other objects are represented by open markers.

drogen envelope. The moderate correlation in hydrogen lines revealed by our sample (i.e., SN II with slower velocity decay of hydrogen lines tends to have a smaller a/e ratio) favours the above explanation and also favours the traditional consensus that those traditionally classified SNe IIL likely have smaller hydrogen envelope mass at SN explosion.

If SNe IIL are formed by single stars, less hydrogen envelope mass (larger mass loss) could point to higher progenitor mass than SNe IIP (Smartt 2009) or high progenitor metallicity at which mass loss is strong enough to remove much of the hydrogen envelope (Heger et al. 2003). Direct observations on progenitor stars of SNe IIL are rare and the estimated masses

have large uncertainties. Nevertheless, Valenti et al. (2016) proposed that SNe IIL appear not to come from more massive progenitors than SNe IIP. Moreover, single stars with enough metallicity will be so massive and they tend to form black-holes by fallback with weak supernovae (Heger et al. 2003). If part of SNe IIL do not have larger progenitor mass than SNe IIP, then it is possible that they originate from binary system and the mass transfer in binaries may play important roles in stripping part of the hydrogen shell. In future works, we intend to discuss the lightcurve properties and the correlations between spectral and photometric parameters, as well as the SN environment, aiming to understand the SN progenitor and its explosion physics.

7 CONCLUSIONS

In this work, we present a compilation of the optical spectra of SNe IIP/IIL observed over the past decade by the Tsinghua Supernova group. The sample consists 206 unreleased spectra for 104 SNe II, covering the phases from ~ 1 d to ~ 200 d after the explosion. Among 49 objects with spectra obtained within 10 days after explosion, two objects (SN 2013ac and SN 2016aqw) are found to show possible flash-ionized emission lines, including narrow lines of H α , H β , HeI 5876, 7065, and HeII 4686. Prominent HV features of hydrogen are detected in six objects and they show different line profiles. Two are shallower and three are deeper. Two HV features are found to likely exist in the blue side of both H α and H β in the $t \sim 76.2$ d spectrum of SN 2013ab. Based on the diversity of line profiles and multiple components, we suggested that CSM interactions could be at least a partial origin of HV features.

The pEW of absorption component of H α in our sample can reach at ~ 100 Å and the emission component can reach at ~ 300 Å in the first ~ 140 days. For individual object, the pEW of Balmer and metal lines show large scatter in the evolution, but we do not find definitive distinctions to separate SNe IIP from SNe IIL. A power-law function is used to fit the velocity evolution in order to estimate the velocity at 50 days after the explosion; moreover, the power-law exponent can be used to describe the velocity decay rate at the same time. For our sample, we found that SNe II with higher velocities during plateau phase show slower velocity evolution for H β . Moreover, the velocity decay rate of hydrogen (i.e., $n_{\text{H}\alpha}$ and $n_{\text{H}\beta}$) have a moderate correlation with the a/e of H α . SNe II with smaller velocity gradient of hydrogen lines tend to have smaller a/e ratios as well, suggesting the progenitors of those SNe II having less amount of hydrogen kept in the stellar envelope before explosion. Photometric parameters, as well as SN environment, will be discussed in future works, in order to understand the observational diversity of SNe II and the mechanisms responsible for these diversities.

ACKNOWLEDGEMENTS

We acknowledge the support of the staff of the Lijiang 2.4 m and Xinglong 2.16-m telescopes. This work is supported by the National Natural Science Foundation of China (NSFC grants 12288102, 12033002 and 11633002) and the Tencent Xplorer Prize. J. Zhang is supported by the National Key R&D Program of China (2021YFA1600404), the National

Natural Science Foundation of China (12173082), the Yunnan Province Foundation (202201AT070069), the Top-notch Young Talents Program of Yunnan Province, the Light of West China Program provided by the Chinese Academy of Sciences, and the International Centre of Supernovae, Yunnan Key Laboratory (202302AN360001). This work was supported by International Centre of Supernovae, Yunnan Key Laboratory (No. 202302AN360001). Y.-Z. Cai is supported by the National Natural Science Foundation of China (NSFC, Grant No. 12303054). This work is supported by the Strategic Priority Research Program of the Chinese Academy of Sciences, Grant No. XDB0550100. This work is supported supported by the National Natural Science Foundation of China (Grant Nos. 12090041, 12090040). This work was partially supported by the Open Project Program of the Key Laboratory of Optical Astronomy, National Astronomical Observatories, Chinese Academy of Sciences. The LJT is jointly operated and administrated by Yunnan Observatories and the Center for Astronomical MegaScience (CAS). Funding for the LJT has been provided by Chinese Academy of Sciences and the Peoples Government of Yunnan Province.

DATA AVAILABILITY

The data underlying this article are available in the article and in its online supplementary material. All the spectra have been uploaded to the webpage of WISEREP (<https://www.wiserep.org>) and Zenodo (<https://doi.org/10.5281/zenodo.10466160>)

REFERENCES

- Anderson J. P., et al., 2014, *ApJ*, **786**, 67
 Barbarino C., et al., 2015, *MNRAS*, **448**, 2312
 Barbon R., Ciatti F., Rosino L., 1979, *A&A*, **72**, 287
 Baron E., et al., 2000, *ApJ*, **545**, 444
 Bartunov O. S., Blinnikov S. I., 1992, *Soviet Astronomy Letters*, **18**, 43
 Blondin S., Tonry J. L., 2007, *ApJ*, **666**, 1024
 Bose S., et al., 2013, *MNRAS*, **433**, 1871
 Bose S., et al., 2015, *MNRAS*, **450**, 2373
 Bose S., et al., 2021, *MNRAS*, **503**, 3472
 Branch D., Baron E., Jeffery D. J., 2001, arXiv e-prints, [pp astro-ph/0111573](https://arxiv.org/abs/astro-ph/0111573)
 Chugai N. N., Chevalier R. A., Utrobin V. P., 2007, *ApJ*, **662**, 1136
 Dall’Ora M., et al., 2014, *ApJ*, **787**, 139
 Elmhamdi A., et al., 2003, *MNRAS*, **338**, 939
 Evans J., 1996, *Straightforward Statistics for the Behavioral Sciences*, Pacific Grove, CA: Brooks/Cole Publishing
 Fan Y.-F., Bai J.-M., Zhang J.-J., Wang C.-J., Chang L., Xin Y.-X., Zhang R.-L., 2015, *Research in Astronomy and Astrophysics*, **15**, 918
 Fan Z., et al., 2016, *PASP*, **128**, 115005
 Faran T., et al., 2014a, *MNRAS*, **442**, 844
 Faran T., et al., 2014b, *MNRAS*, **445**, 554
 Filippenko A. V., 1997, *ARA&A*, **35**, 309
 Filippenko A. V., Matheson T., Ho L. C., 1993, *ApJ*, **415**, L103
 Fraser M., et al., 2012, *ApJ*, **759**, L13
 Gal-Yam A., et al., 2014, *Nature*, **509**, 471
 Galbany L., et al., 2016, *AJ*, **151**, 33
 Gutiérrez C. P., et al., 2014, *ApJ*, **786**, L15
 Gutiérrez C. P., et al., 2017a, *ApJ*, **850**, 89
 Gutiérrez C. P., et al., 2017b, *ApJ*, **850**, 90

Hamuy M., Suntzeff N. B., Gonzalez R., Martin G., 1988, *AJ*, **95**, 63

Heger A., Fryer C. L., Woosley S. E., Langer N., Hartmann D. H., 2003, *ApJ*, **591**, 288

Hendry M. A., et al., 2005, *MNRAS*, **359**, 906

Hosseinzadeh G., et al., 2018, *ApJ*, **861**, 63

Huang F., et al., 2015, *ApJ*, **807**, 59

Jerkstrand A., Fransson C., Maguire K., Smartt S., Ergon M., Spyromilio J., 2012, *A&A*, **546**, A28

Khazov D., et al., 2016, *ApJ*, **818**, 3

Kilpatrick C. D., Foley R. J., 2018, *MNRAS*, **481**, 2536

Kochanek C. S., et al., 2017, *MNRAS*, **467**, 3347

Li W., Van Dyk S. D., Filippenko A. V., Cuillandre J.-C., Jha S., Bloom J. S., Riess A. G., Livio M., 2006, *ApJ*, **641**, 1060

Lin H., et al., 2021, *MNRAS*, **505**, 4890

Litvinova I. I., Nadezhin D. K., 1983, *Ap&SS*, **89**, 89

Maguire K., et al., 2012, *MNRAS*, **420**, 3451

Maund J. R., Smartt S. J., Danziger I. J., 2005, *MNRAS*, **364**, L33

Minkowski R., 1941, *PASP*, **53**, 224

Moriya T. J., Pruzhinskaya M. V., Ergon M., Blinnikov S. I., 2016, *MNRAS*, **455**, 423

Morozova V., Piro A. L., Renzo M., Ott C. D., Clausen D., Couch S. M., Ellis J., Roberts L. F., 2015, *ApJ*, **814**, 63

Nakaoka T., et al., 2018, *ApJ*, **859**, 78

Pastorello A., et al., 2009, *MNRAS*, **394**, 2266

Patat F., Barbon R., Cappellaro E., Turatto M., 1994, *A&A*, **282**, 731

Pignata G., 2015, in IAU General Assembly. p. 2255784

Popov D. V., 1993, *ApJ*, **414**, 712

Rodríguez Ó., et al., 2020, *MNRAS*, **494**, 5882

Rubin A., et al., 2016, *ApJ*, **820**, 33

Rui L., et al., 2019, *MNRAS*, **485**, 1990

Sahu D. K., Anupama G. C., Sridivya S., Muneer S., 2006, *MNRAS*, **372**, 1315

Sanders N. E., et al., 2015, *ApJ*, **799**, 208

Schlafly E. F., Finkbeiner D. P., 2011, *ApJ*, **737**, 103

Schlegel E. M., 1990, *MNRAS*, **244**, 269

Schlegel E. M., 1996, *AJ*, **111**, 1660

Shivvers I., Groh J. H., Mauerhan J. C., Fox O. D., Leonard D. C., Filippenko A. V., 2015, *ApJ*, **806**, 213

Silverman J. M., et al., 2012, *MNRAS*, **425**, 1789

Silverman J. M., et al., 2017, *MNRAS*, **467**, 369

Smartt S. J., 2009, *ARA&A*, **47**, 63

Smartt S. J., Eldridge J. J., Crockett R. M., Maund J. R., 2009, *MNRAS*, **395**, 1409

Smith N., 2017, *Interacting Supernovae: Types IIin and Ibn*. p. 403, doi:10.1007/978-3-319-21846-5_38

Spiro S., et al., 2014, *MNRAS*, **439**, 2873

Szalai T., et al., 2019, *ApJ*, **876**, 19

Takáts K., Vinkó J., 2012, *MNRAS*, **419**, 2783

Takáts K., et al., 2014, *MNRAS*, **438**, 368

Tody D., 1986, in Crawford D. L., ed., *Society of Photo-Optical Instrumentation Engineers (SPIE) Conference Series Vol. 627, Instrumentation in astronomy VI*. p. 733, doi:10.1117/12.968154

Tody D., 1993, in Hanisch R. J., Brissenden R. J. V., Barnes J., eds, *Astronomical Society of the Pacific Conference Series Vol. 52, Astronomical Data Analysis Software and Systems II*. p. 173

Valenti S., et al., 2016, *MNRAS*, **459**, 3939

Van Dyk S. D., Li W., Filippenko A. V., 2003, *PASP*, **115**, 1289

Van Dyk S. D., et al., 2012, *ApJ*, **756**, 131

Van Dyk S. D., et al., 2019, *ApJ*, **875**, 136

Vinkó J., et al., 2006, *MNRAS*, **369**, 1780

Xiang D., et al., 2023, *MNRAS*, **520**, 2965

Yaron O., et al., 2017, *Nature Physics*, **13**, 510

Zhang J., et al., 2014, *ApJ*, **797**, 5

Zhang J., et al., 2020, *MNRAS*, **498**, 84

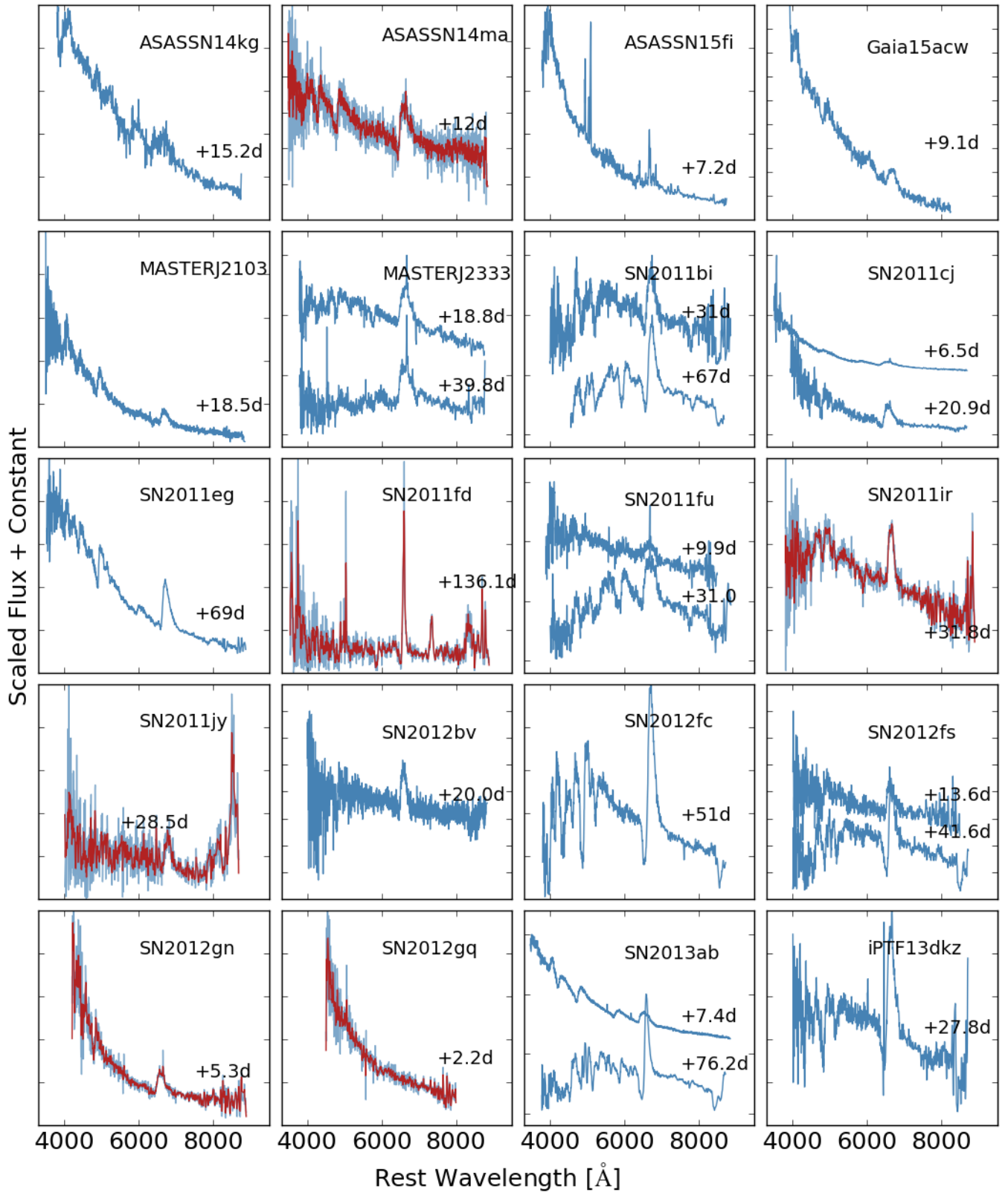
Zhang J., et al., 2023, *Science Bulletin*, **68**, 2548

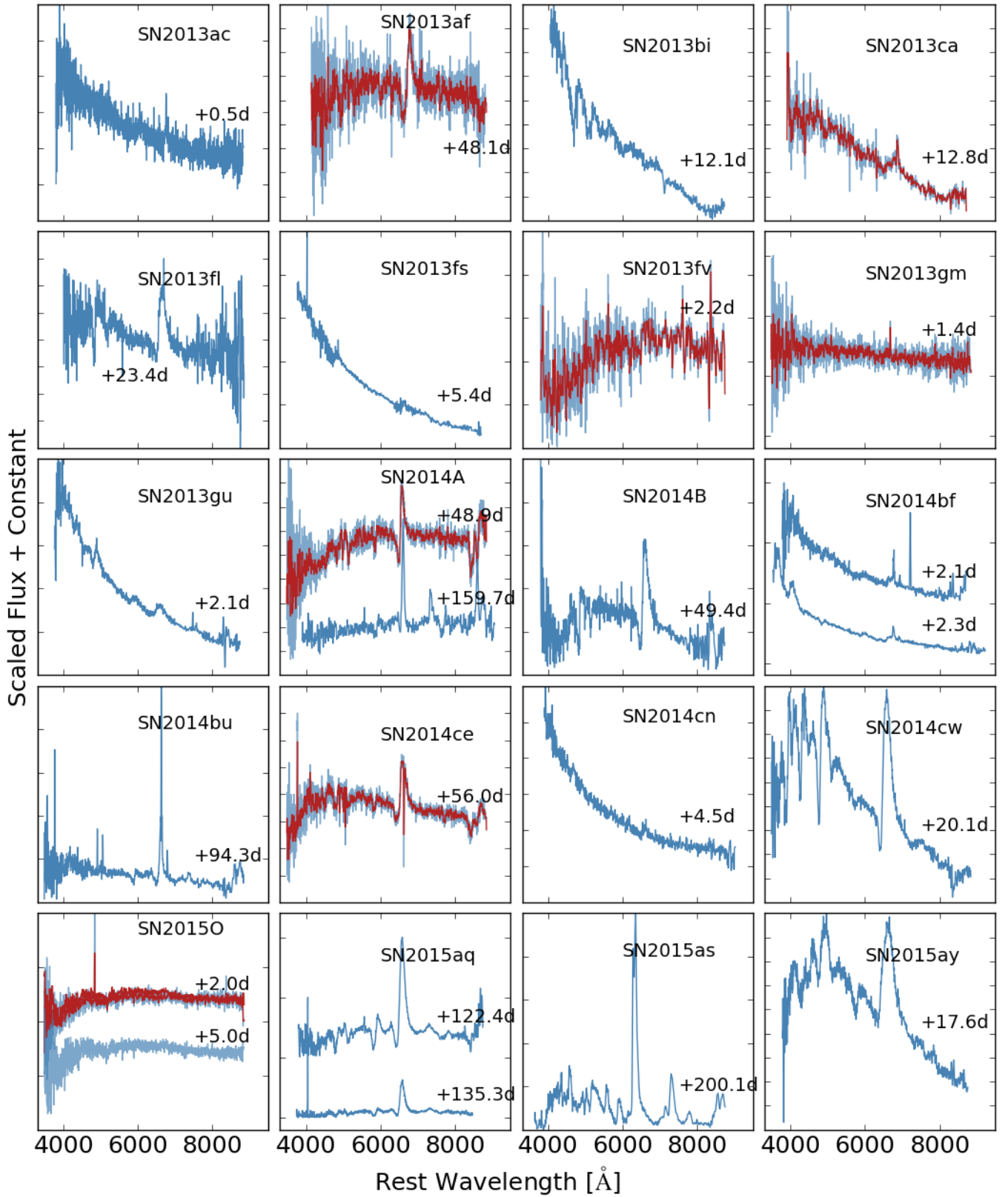
de Jaeger T., et al., 2015, *ApJ*, **815**, 121

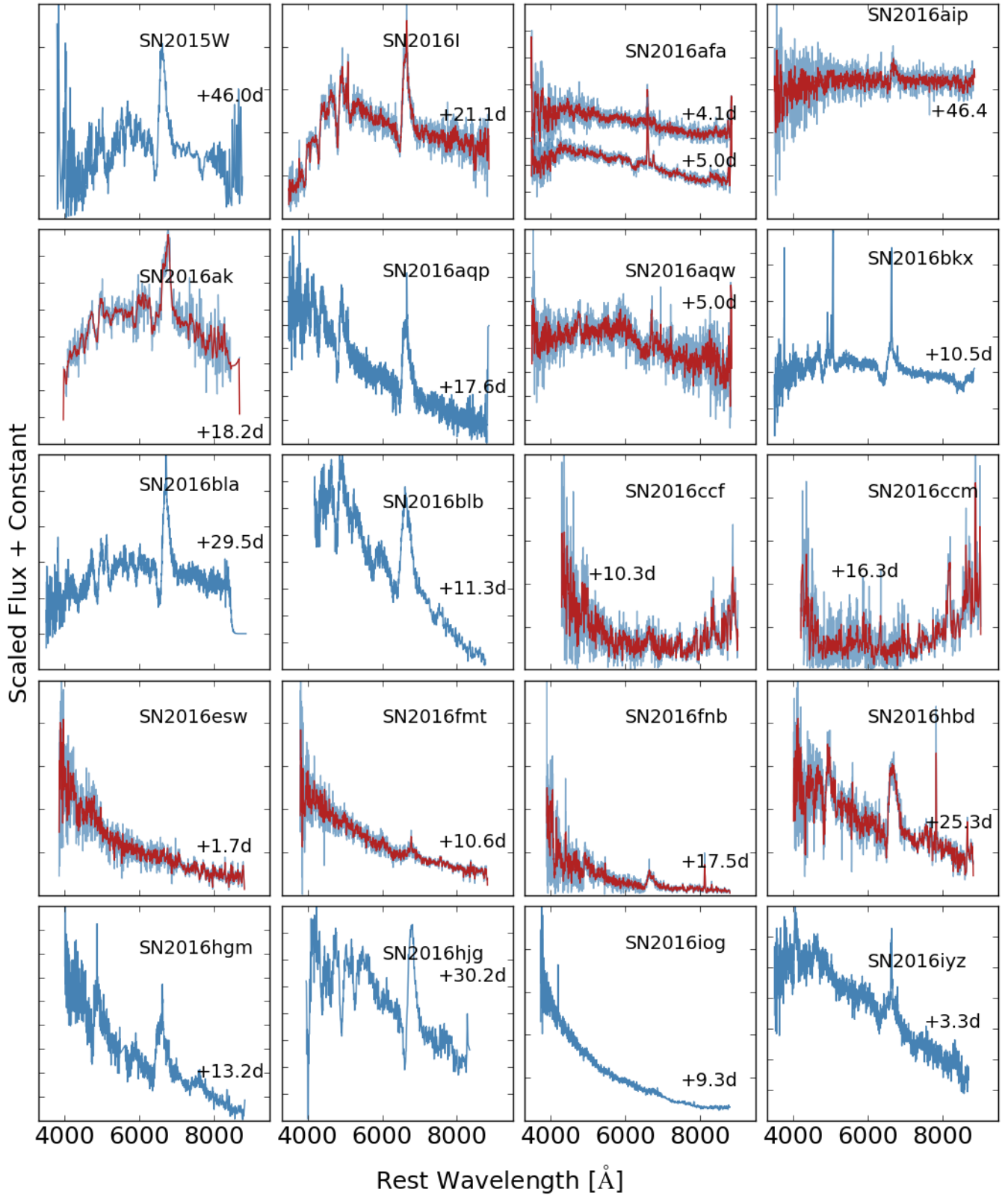
de Jaeger T., et al., 2018, *MNRAS*, **478**, 3776

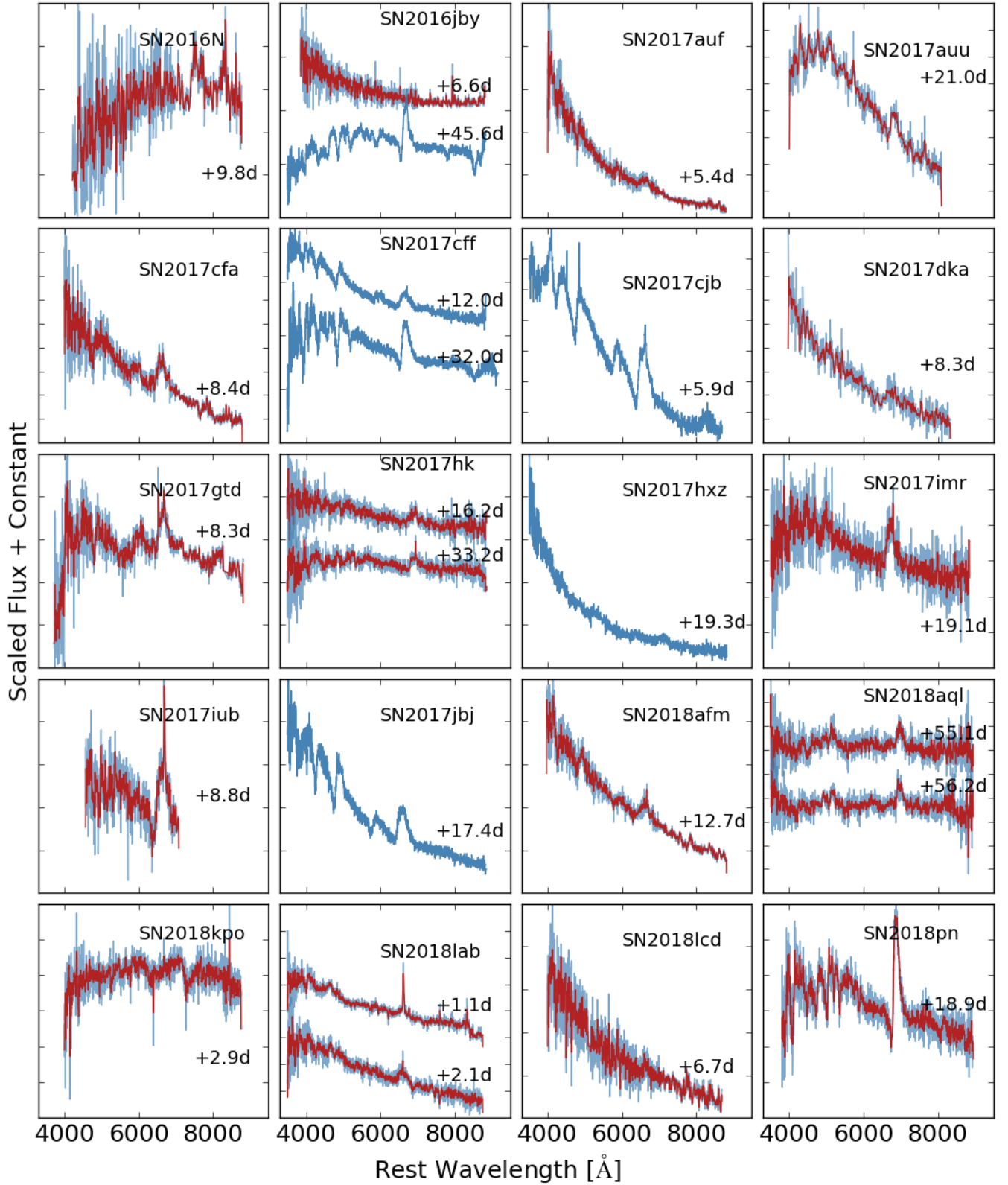
de Jaeger T., et al., 2019, *MNRAS*, **490**, 2799

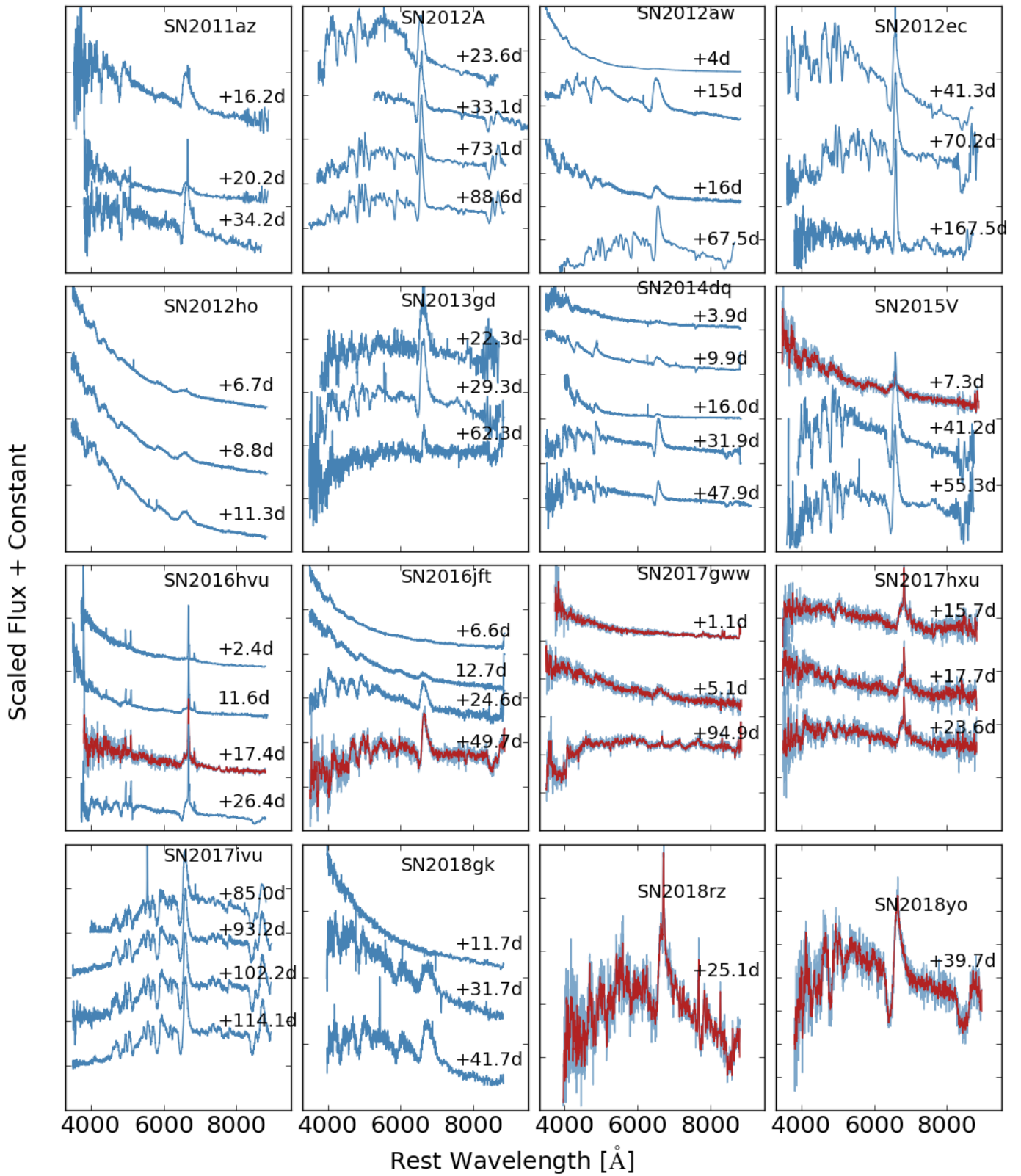
APPENDIX A: SOME EXTRA MATERIAL











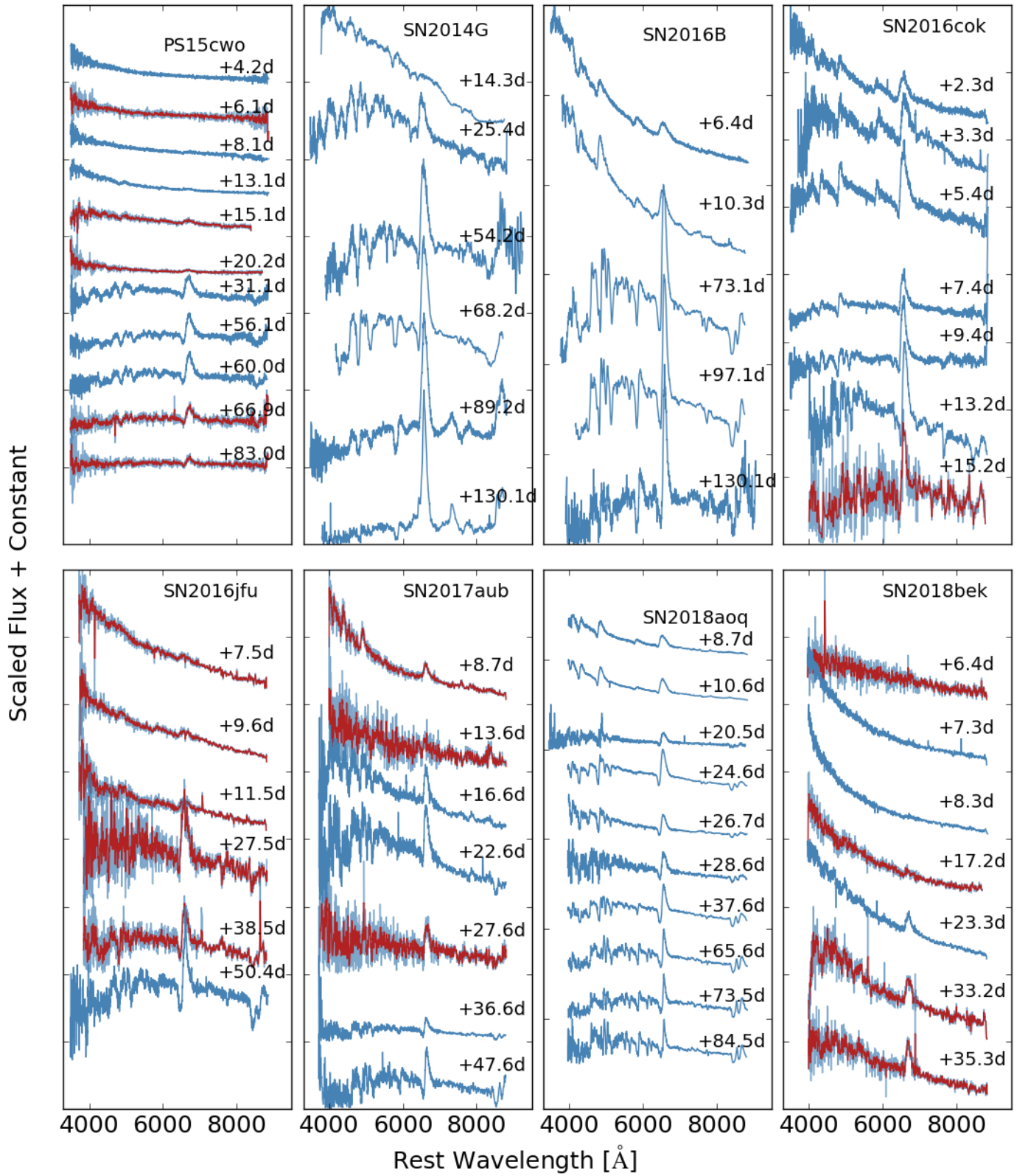


Figure A-1. Spectral evolution of our SN II sample presented in this work.

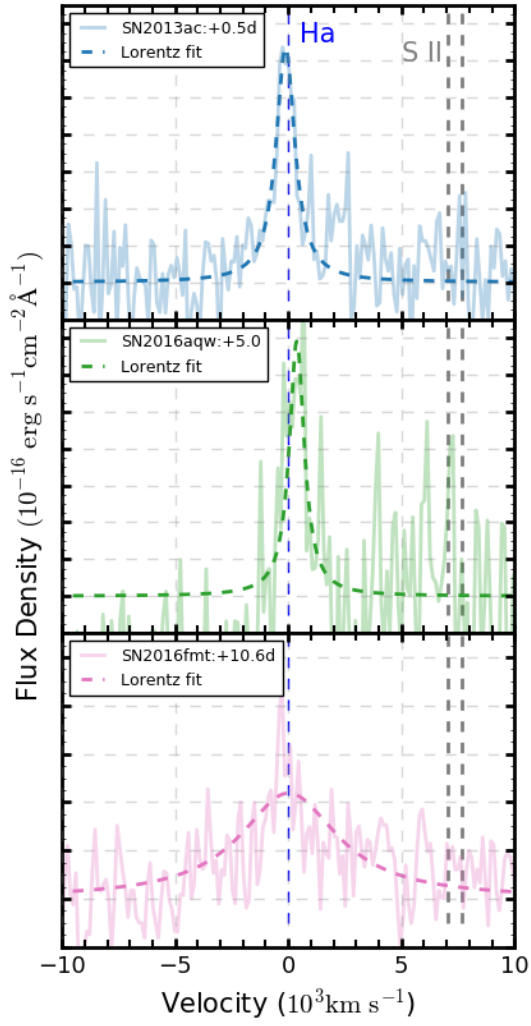


Figure A2. The $H\alpha$ line profile in the spectrum of SN2013ac, SN 2016aqw and SN 2016fmt. The dashed lines are the Lorentzian fits for the $H\alpha$ line profile.

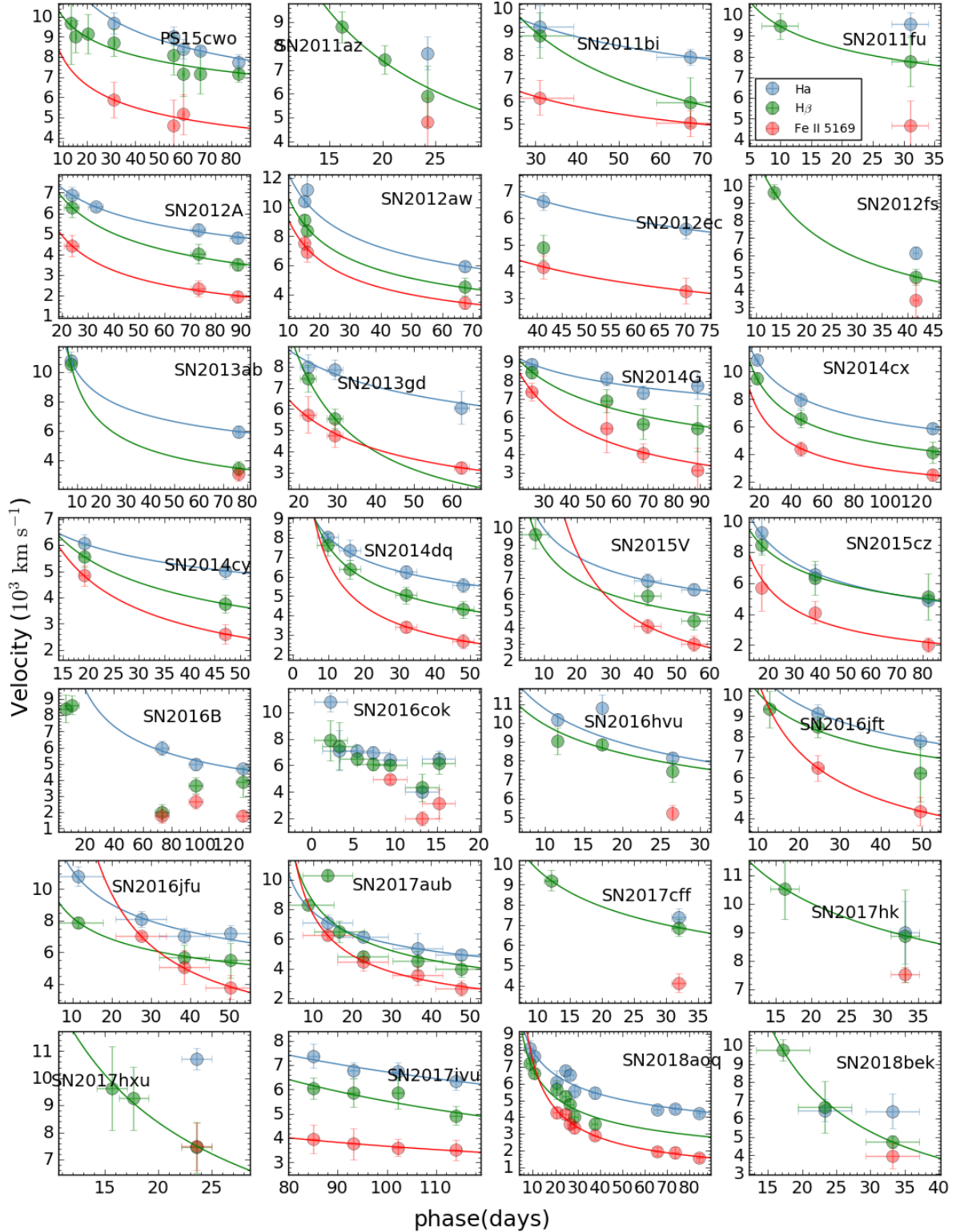


Figure A3. The velocity evolution inferred from H α (blue dots), H β (green dots) and Fe II 5169 (red dots) lines in the spectra of our sample of SNe II. Overplotted are the power-law fitting to the observed velocity evolution. We must notice that the power-law exponent of our sample has larger errors, and this is due to bad spectral sampling.

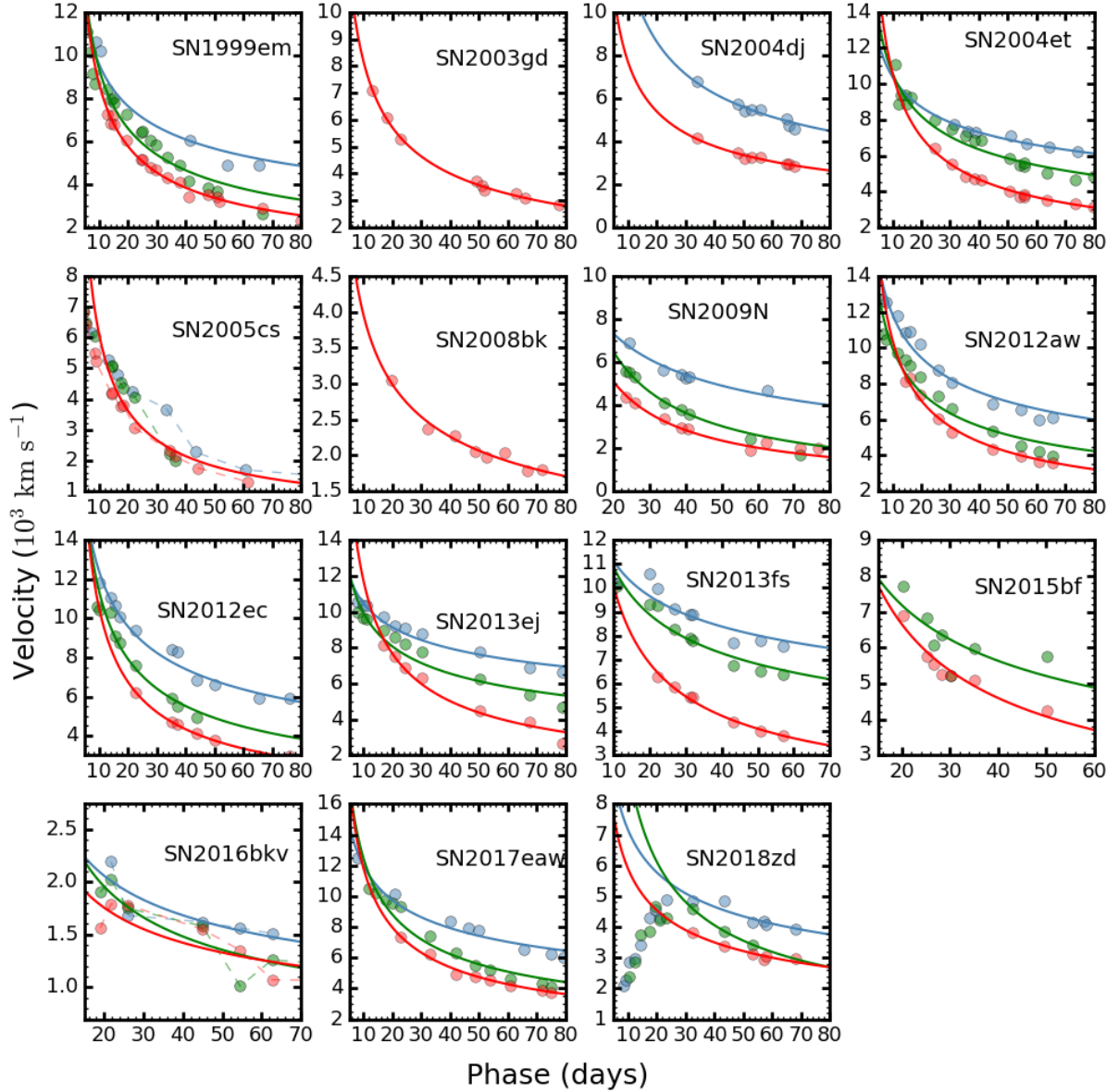
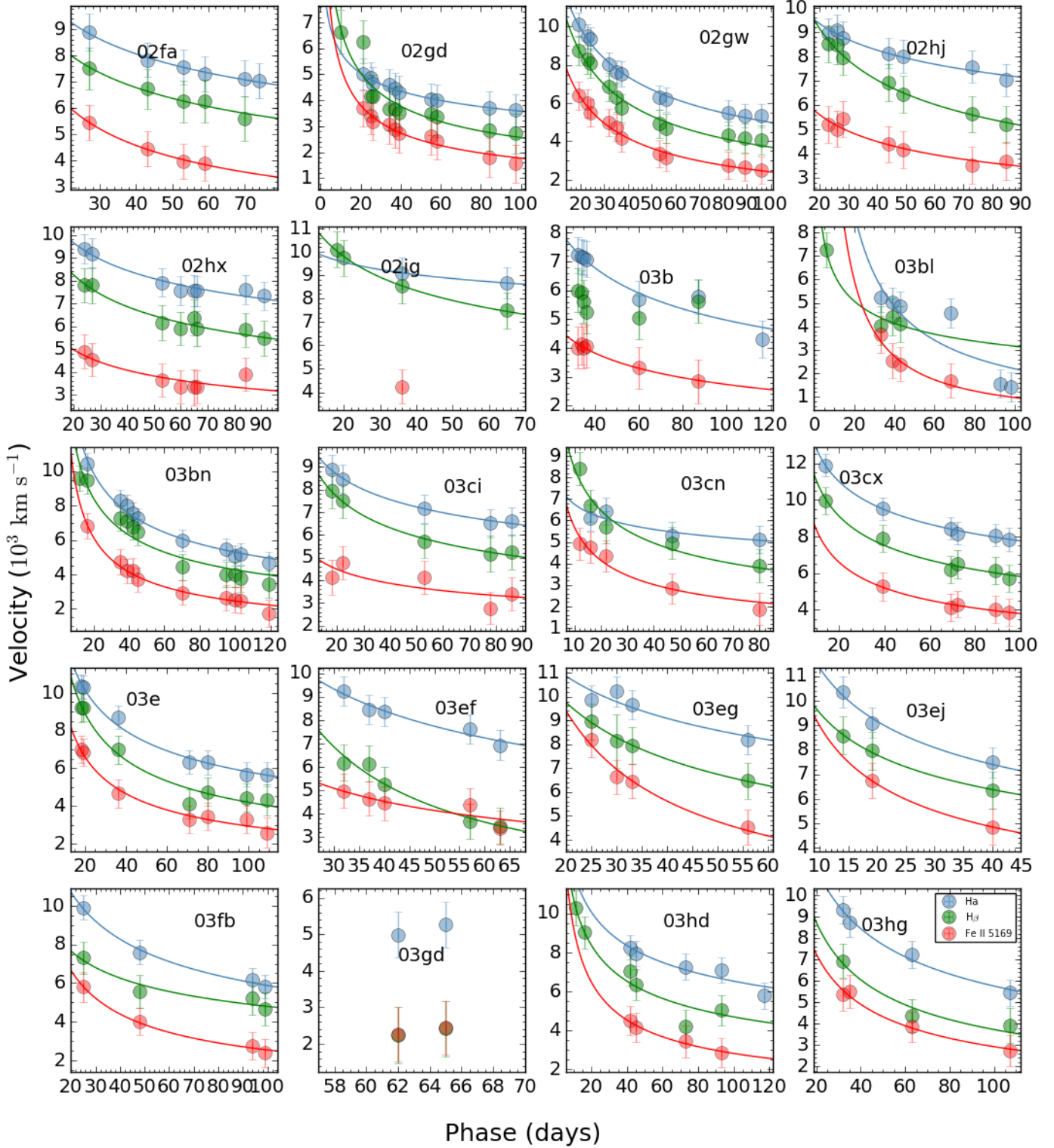
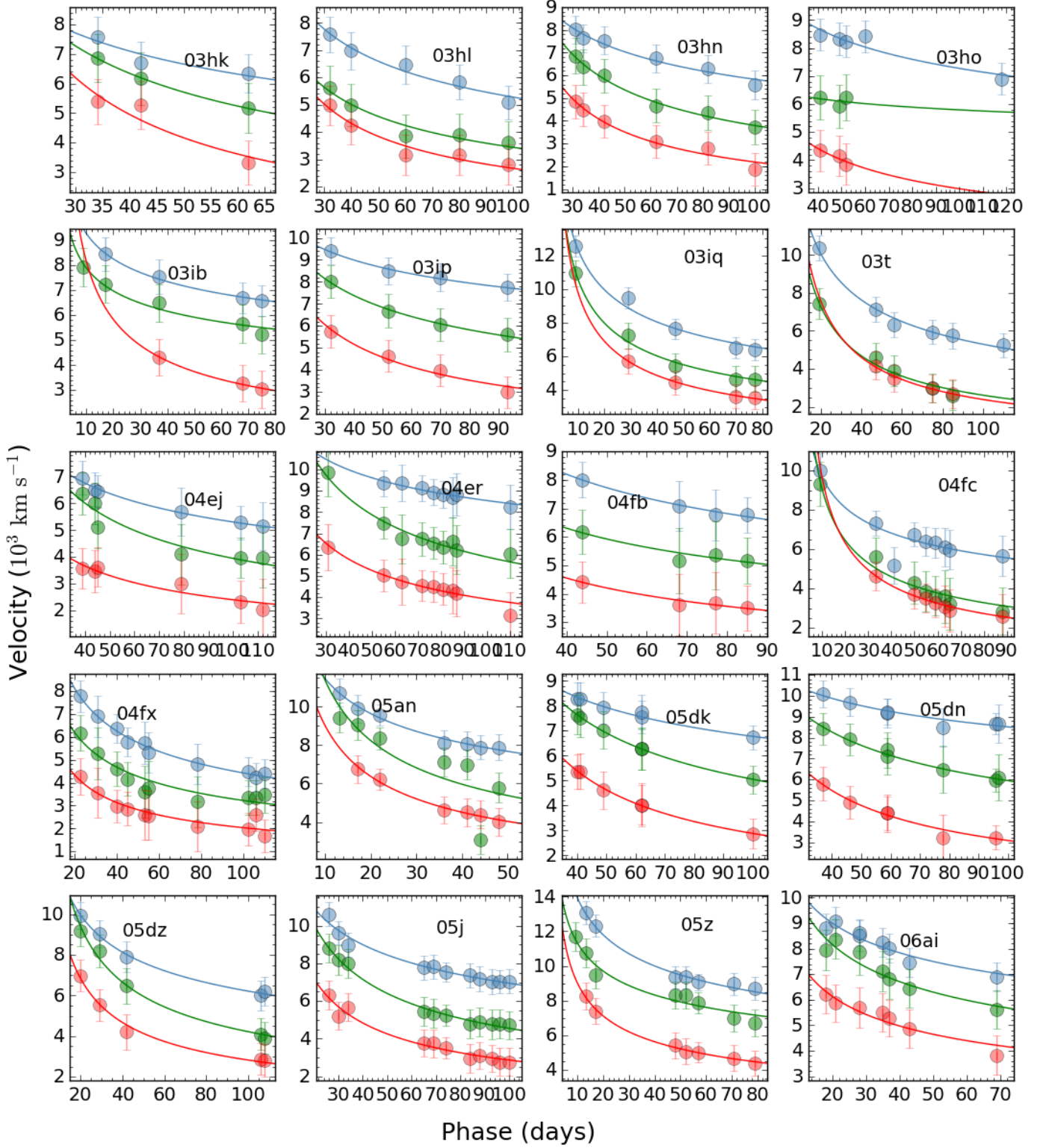
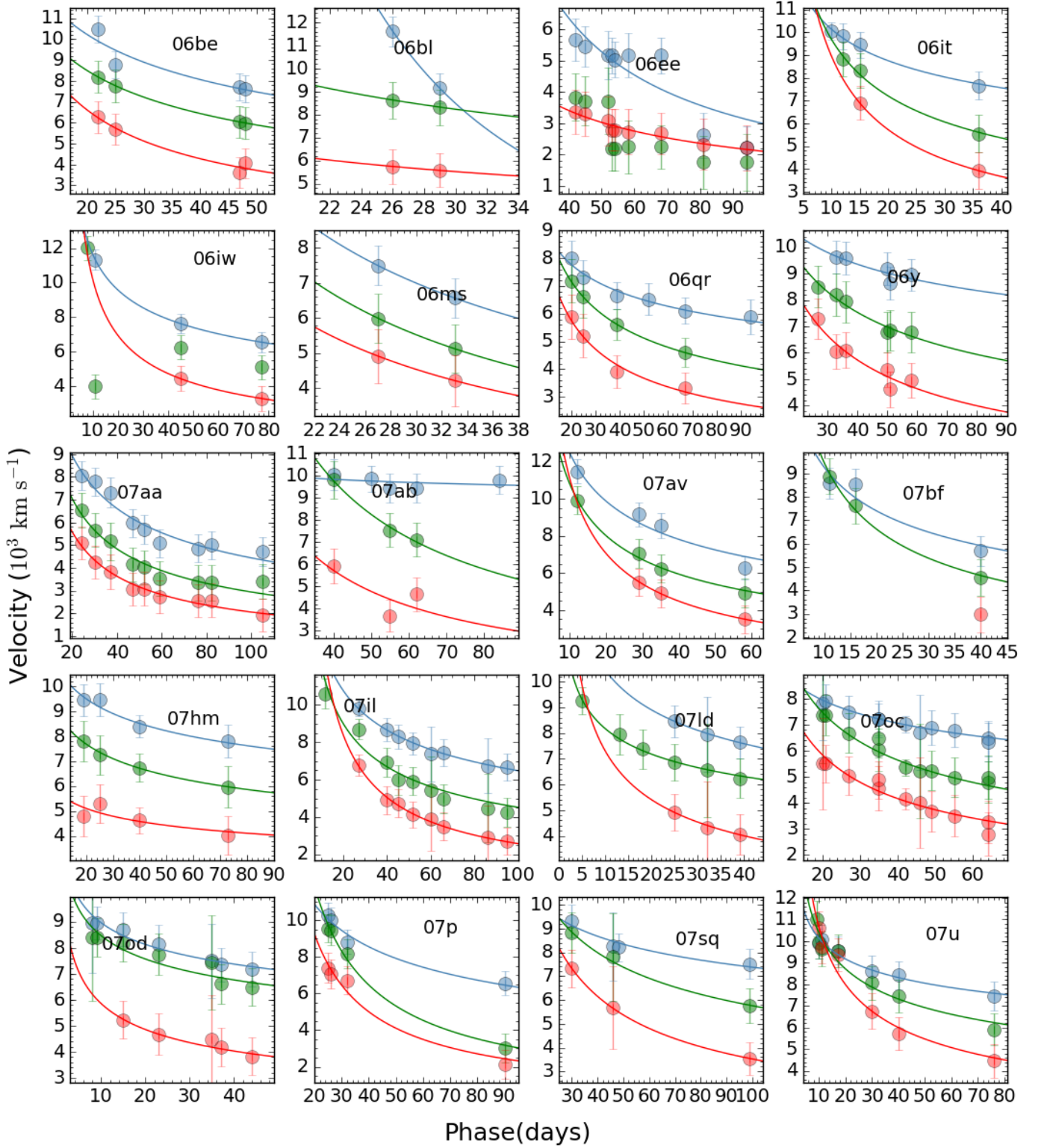
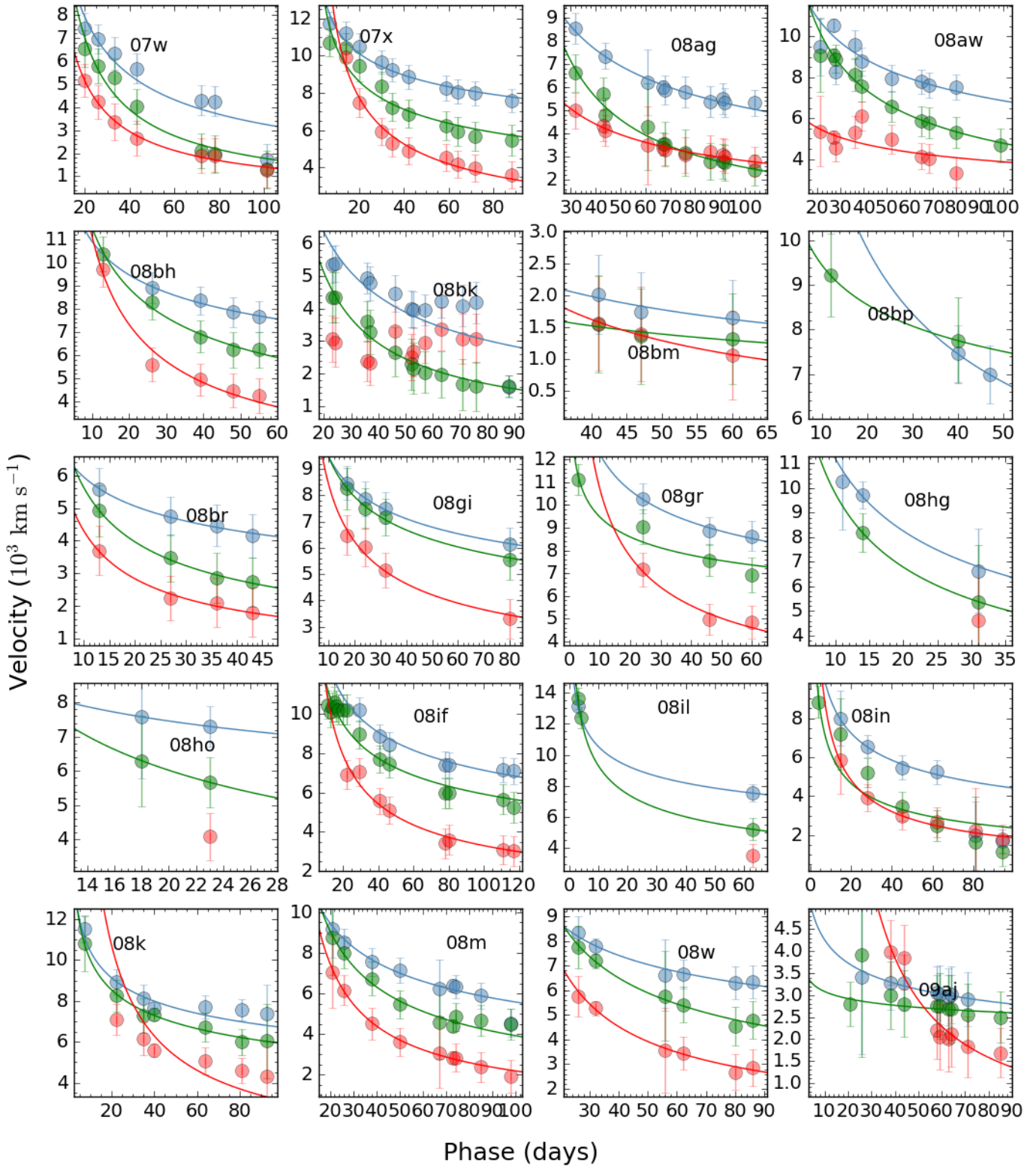


Figure A4. Same as Figure A3, but for the well-studied sample in literature. The newly added sample include the typical SNe IIP like SN 1999em (Elmhamdi et al. 2003; Takáts & Vinkó 2012), SN 2004dj (Vinkó et al. 2006), SN 2012ec (Barbarino et al. 2015), SN2004et (Sahu et al. 2006; Takáts & Vinkó 2012), SN 2012aw (Bose et al. 2013) and SN 2017eaw (Van Dyk et al. 2019; Szalai et al. 2019); fast declining samples of SN 2013ej (Huang et al. 2015) and SN 2015bf (Lin et al. 2021); the low-luminosity, low-velocity objects of SN 2003gd (Hendry et al. 2005), SN 2005cs (Pastorello et al. 2009; Takáts & Vinkó 2012), SN 2008bk (Pignata 2015) and SN2016bkv (Nakaoka et al. 2018); SN 2009N (Takáts et al. 2014), which link normal and subluminous SNe IIP; and SN 2018zd (Zhang et al. 2020). Among these objects, SN 2013fs, SN 2015bf, SN 2016bkv and SN 2018zd have flash ionized features at early phases, which indicate massive CSM and therefore larger mass loss rate of progenitor shortly before the SN explosion.









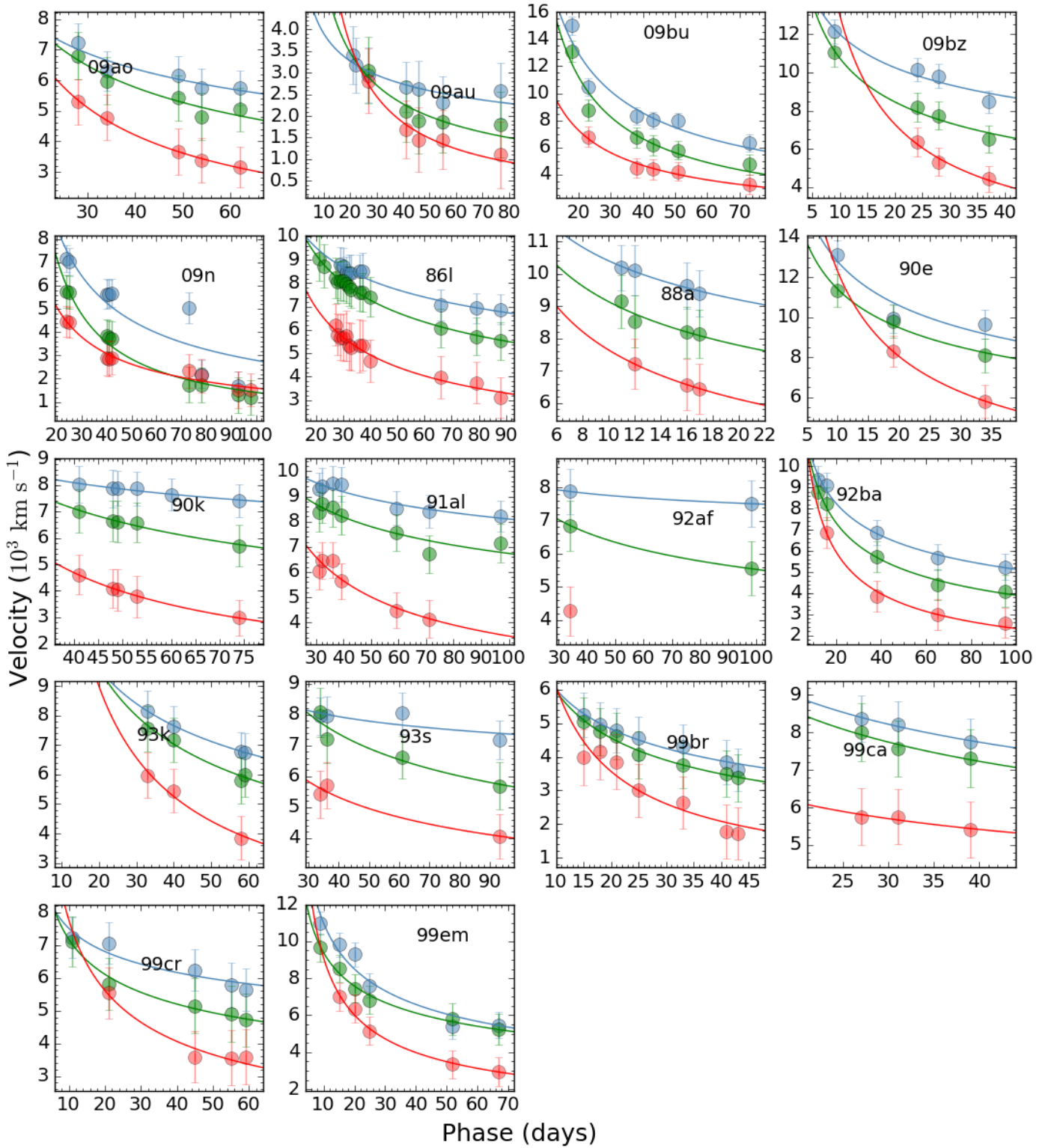


Figure A5. Same as Figure A3 and Figure A4, but for the SN II sample in Gutiérrez et al. (2017a).

SN II sample continue									
SN	RA	DEC	Host galaxy	Redshift	$E(B - V)_{mw}$	Last non-detection	First discovery	Explosion date	
SN2018lab	06:16:26.53	-21:22:32.46	IC 2163	0.009223	0.077	58480.13	58481.13	58480.6(0.5) ^a	
SN2018led	01:51:10.81	-03:29:26.87	MCG -01-05-42	0.007	0.026	58480.33	58481.27	58480.8(0.5) ^a	
SN2018pn	07:56:11.30	45:31:36.40	...	0.048	0.0469			58154.6	
SN2018rz	14:27:11.44	-02:16:10.07	NGC 5618	0.02379	0.0464	58130.7	58142.86	58136.8(6.1) ^a	
SN2018yo	12:41:11.14	-01:35:20.40	UGC 7840	0.0134	0.0273	58140	58175.42	58138.1(3.6) ^b	

a:Explosion date estimated by midpoints between the last non-detection and the first discovery.

b:Explosion date estimated by matching spectral templates via the SNID.

c:First discovery was used as explosion date.

d:(de Jaeger et al. 2019); e:(Valenti et al. 2016); f:(Rubin et al. 2016); g:(Dall'Ora et al. 2014).

h:(Bose et al. 2015); i:(Yaron et al. 2017); j:(de Jaeger et al. 2018); k:(Bose et al. 2021).

Table A2: Journal of Spectroscopic Observations of our SN II sample.

SN	Obs. date	JD	Phase ^a (Days)	Instrument	Resolution($\text{\AA} \text{ pix}^{-1}$)	Wavelength range(\AA)
ASASSN-14kg	20141123	2456985.18	+15.2	BFOSC	4.42	3800-8800
ASASSN-14ma	20141214	2457006.98	+12.0d	YFOSC	2.93	3500-8900
ASASSN-15fi	20150324	2457106.24	>7.2d	BFOSC	4.42	3800-8800
Gaia15acw	20141214	2457006.25	+9.1	YFOSC	7.91	3900-8300
iPTF13dkz	20131011	2456576.21	+27.8	BFOSC	4.42	4000-8700
MASTER_J2103	20141108	2456970.98	+18.5	YFOSC	2.93	3500-8900
MASTER_J2333	20151013	2457309.00	+18.8	BFOSC	4.42	3800-8800
MASTER_J2333	20151103	2457330.01	+39.8	BFOSC	18.3	3800-8800
PS15cwo	20151111	2457339.31	+4.2	YFOSC	2.93	3500-8900
PS15cwo	20151114	2457341.18	+6.1	YFOSC	2.93	3500-8900
PS15cwo	20151115	2457343.18	+8.1	YFOSC	2.93	3500-8900
PS15cwo	20151120	2457348.22	+13.1	YFOSC	2.93	3500-8900
PS15cwo	20151123	2457350.17	+15.1	YFOSC	2.93	3500-8400
PS15cwo	20151127	2457355.30	+20.2	YFOSC	2.93	3500-8700
PS15cwo	20151208	2457366.19	+31.1	YFOSC	2.93	3500-8900
PS15cwo	20160102	2457391.16	+56.1	YFOSC	2.93	3500-8900
PS15cwo	20160106	2457395.11	+60.0	YFOSC	2.93	3500-8900
PS15cwo	20160113	2457401.99	+66.9	YFOSC	2.93	3500-8900
PS15cwo	20160129	2457418.14	+83.0	YFOSC	2.93	3500-8900
SN2011az	20110403	2455655.20	>16.2	OMR	4.8	3500-8900
SN2011az	20110408	2455659.18	>20.2	OMR	4.8	3500-8900
SN2011az	20110422	2455673.18	>34.2	BFOSC	4.42	3800-8700
SN2011bi	20110408	2455659.30	+31	OMR	4.8	4000-8900
SN2011bi	20110513	2455695.28	+67.0	BFOSC	4.42	4600-8700
SN2011cj	20110513	2455695.15	+6.5	BFOSC	4.42	3500-8700
SN2011cj	20110527	2455709.50	+20.9	BFOSC	4.42	3900-8700
SN2011eg	20110930	2455834.98	>69	OMR	4.8	3500-8900
SN2011fd	20111223	2455919.08	+136.1	BFOSC	4.42	3500-8900
SN2011fu	20110930	2455835.13	+9.9	OMR	4.8	3900-8500
SN2011fu	20111021	2455856.21	+31.0	OMR	16.2	4000-8900
SN2011ir	20111223	2455918.30	>31.8	OMR	4.8	3800-8900
SN2011jy	20120127	2455953.50	>28.5d	BFOSC	18.2	4000-8700
SN2012A	20120127	2455953.50	+23.6	BFOSC	4.42	3700-8700
SN2012A	20120204	2455963.03	+33.1	YFOSC	2.93	5300-9600
SN2012A	20120316	2456003.07	+73.1	OMR	4.8	3700-8900
SN2012A	20120401	2456018.50	+88.6	YFOSC	2.93	3500-8900
SN2012aw	20120320	2456006.50	+4	YFOSC	2.93	3500-8800
SN2012aw	20120331	2456017.50	+15	YFOSC	2.93	3500-8800
SN2012aw	20120401	2456018.50	+16	YFOSC	2.93	3500-8900
SN2012aw	20120522	2456070.03	+67.5	BFOSC	4.42	3900-8700
SN2012bv	20120429	2456046.02	>20.0	YFOSC	2.93	4000-8800
SN2012ec	20120914	2456184.25	+41.3	BFOSC	4.42	3600-8700
SN2012ec	20121012	2456213.24	+70.2	OMR	4.8	3600-8900
SN2012ec	20130118	2456310.50	+167.5	BFOSC	4.42	3800-8700
SN2012fc	20121109	2456241.04	>51.0	BFOSC	4.42	3800-8700
SN2012fs	20121012	2456213.10	+13.6	OMR	4.8	4000-8500
SN2012fs	20121109	2456241.11	+41.6	BFOSC	4.42	4000-8700
SN2012gn	20121116	2456248.32	>5.3	OMR	4.8	4200-8900
SN2012gq	20121116	2456248.23	>2.2	OMR	4.8	4500-8000
SN2012ho	20121207	2456268.98	+6.7	YFOSC	2.93	3500-8800
SN2012ho	20121210	2456271.00	+8.8	YFOSC	2.93	3500-8900
SN2012ho	20121212	2456273.50	+11.3	YFOSC	2.93	3500-8900
SN2013ab	20130225	2456347.36	+7.4	YFOSC	2.93	3500-8800
SN2013ab	20130503	2456416.23	+76.2	BFOSC	2.93	3500-8800
SN2013ac	20130216	2456339.46	>0.5	YFOSC	2.93	3800-8800
SN2013af	20130302	2456354.07	+48.1	YFOSC	2.93	4200-8900
SN2013bi	20130405	2456388.14	>12.1	BFOSC	4.42	4100-8700
SN2013ca	20150503	2456416.07	+12.8	BFOSC	4.42	3900-8700
SN2013fi	20130925	2456560.97	+23.4	OMR	4.8	4000-8900
SN2013fs	20131011	2456577.06	+5.4	BFOSC	4.42	3800-8700
SN2013fv	20131014	2456579.20	>2.2	BFOSC	4.42	3800-8700
SN2013gd	20131129	2456626.14	+22.3	BFOSC	4.42	3800-8700
SN2013gd	20131206	2456633.14	+29.3	BFOSC	4.42	3800-8700
SN2013gd	20140107	2456666.10	+62.3	YFOSC	2.93	3500-8900
SN2013gm	20131121	2456618.41	>1.4	YFOSC	2.93	3500-8900
SN2013gu	20131206	2456633.09	>2.1	BFOSC	4.42	3800-8700
SN2014A	20140102	2456660.42	+48.9	YFOSC	2.93	3500-8900
SN2014A	20140423	2456771.23	+159.7	YFOSC	7.91	3900-9100
SN2014B	20140104	2456662.38	+49.4	BFOSC	4.42	3800-8700
SN2014Bf	20140524	2456802.17	>2.1	BFOSC	4.42	3800-8700
SN2014Bf	20140524	2456802.31	>2.3	YFOSC	7.91	3500-9200
SN2014bu	20140918	2456919.27	>94.3	OMR	9.6	3500-8800
SN2014ce	20141003	2456934.02	+56.0	YFOSC	2.93	3500-8900
SN2014cn	20140424	2456772.22	+4.5	YFOSC	7.91	3900-9000
SN2014cw	20140918	2456919.07	>20.1	OMR	4.8	3500-8800
SN2014dq	20141019	2456949.98	+3.9	YFOSC	2.93	3500-8800
SN2014dq	20141024	2456956.00	+9.9	YFOSC	2.93	3500-8900
SN2014dq	20141030	2456962.08	+16.0	YFOSC	2.93	4000-8900
SN2014dq	20141116	2456977.99	+31.9	YFOSC	2.93	3500-8900
SN2014dq	20141202	2456993.99	+47.9	YFOSC	2.93	3500-9100
SN2014G	20140127	2456684.26	+14.3	BFOSC	4.42	3800-8800
SN2014G	20140206	2456695.40	+25.4	YFOSC	2.93	3500-8900
SN2014G	20140307	2456724.18	+54.2	OMR	4.8	3900-9200
SN2014G	20140321	2456738.24	+68.2	BFOSC	4.42	4200-8700
SN2014G	20140411	2456759.21	+89.2	YFOSC	2.93	3500-8900
SN2014G	20140522	2456800.05	+130.1	BFOSC	4.42	3800-8700
SN2015aq	20151204	2457361.39	+122.4	BFOSC	4.42	3800-8800
SN2015aq	20151217	2457374.33	+135.3	BFOSC	2.97	3700-8500
SN2015as	20160602	2457542.05	>200.1	BFOSC	5.88	3600-8800
SN2015ay	20151013	2457309.23	+17.6	BFOSC	4.42	3800-8800
SN2015O	20150623	2457197.21	+2.0	YFOSC	2.93	3500-8900
SN2015O	20150626	2457200.19	+5.0	YFOSC	2.93	3500-8900

Journal of Spectroscopic Observations of our SN II sample (continue)						
SN	Obs. date	JD	Phase (Days)	Instrument	Resolution(\AA pix $^{-1}$)	Wavelength range(\AA)
SN2015V	20150406	2457120.28	+7.3	YFOSC	2.93	3500-8900
SN2015V	20150511	2457154.18	+41.2	BFOSC	4.42	3900-8800
SN2015V	20150525	2457168.27	+55.3	BFOSC	27	3600-8700
SN2015W	20150213	2457067.01	+46.0	BFOSC	4.42	3800-8800
SN2016afa	20160213	2457432.46	+4.1	YFOSC	2.93	3500-8900
SN2016afa	20160214	2457433.44	+5.0	YFOSC	2.93	3500-8900
SN2016aip	20160217	2457437.04	+46.4	YFOSC	2.93	3500-8900
SN2016ak	20160118	2457406.33	+18.2	YFOSC	7.91	4000-8700
SN2016aqp	20160226	2457446.02	+17.6	YFOSC	2.93	3500-8900
SN2016aqw	20160303	2457451.36	+5.0	YFOSC	2.93	3500-8900
SN2016B	20160104	2457392.36	+6.4	YFOSC	2.93	3500-8900
SN2016B	20160108	2457396.28	+10.3	BFOSC	4.42	3800-8800
SN2016B	20160311	2457459.13	+73.1	BFOSC	4.42	3800-8800
SN2016B	20160404	2457483.13	+97.1	BFOSC	4.42	4200-8800
SN2016B	20160507	2457516.08	+130.1	OMR	2.4	3900-9100
SN2016bkx	20160325	2457474.11	>10.5	YFOSC	2.93	3500-8900
SN2016bla	20160330	2457478.12	>29.5	YFOSC	2.93	3500-8900
SN2016blb	20160404	2457483.16	+11.3	BFOSC	4.42	4200-8800
SN2016ccf	20160506	2457515.03	>10.3	BFOSC	2.97	4300-9000
SN2016ccm	20160506	2457515.24	>16.3	BFOSC	2.97	4200-9000
SN2016cok	20160528	2457537.12	+2.3	YFOSC	2.93	3500-8900
SN2016cok	20160529	2457538.06	+3.3	BFOSC	6.63	3700-8800
SN2016cok	20160530	2457540.15	+5.4	YFOSC	2.93	3500-8900
SN2016cok	20160601	2457542.17	+7.4	YFOSC	2.93	3500-8900
SN2016cok	20160604	2457544.16	+9.4	YFOSC	2.93	3400-8900
SN2016cok	20160608	2457548.02	+13.2	BFOSC	6.63	4000-8800
SN2016cok	20160610	2457550.04	+15.2	BFOSC	6.63	4000-8800
SN2016esw	20160809	2457610.02	+1.7	BFOSC	2.97	3800-8800
SN2016fnt	20160830	2457631.31	+10.6	BFOSC	2.97	3800-8800
SN2016fmb	20160830	2457631.25	+17.5	BFOSC	2.97	3900-8800
SN2016hbd	20161028	2457690.26	>25.3	BFOSC	2.97	4000-8800
SN2016hgm	20161028	2457690.17	+13.2	BFOSC	2.97	4000-8800
SN2016hjj	20161118	2457712.18	>30.2	YFOSC	7.91	4000-8300
SN2016hvu	20161108	2457700.96	>2.4	BFOSC	2.97	3700-8800
SN2016hvu	20161116	2457710.16	>11.6	YFOSC	2.93	3500-8900
SN2016hvu	20161123	2457715.95	>17.4	BFOSC	2.97	3800-8800
SN2016hvu	20161202	2457724.98	>26.4	BFOSC	2.97	3700-8800
SN2016I	20160113	2457401.43	+21.1	YFOSC	2.93	3500-8900
SN2016iog	20161202	2457725.39	+9.3	BFOSC	2.97	3700-8800
SN2016iyz	20161222	2457745.23	+3.3	YFOSC	2.93	3500-8700
SN2016jby	20161228	2457751.31	+6.6	BFOSC	2.97	3900-8800
SN2016jby	20170205	2457790.35	+45.6	YFOSC	2.93	3500-8900
SN2016jft	20161231	2457755.23	+6.6	YFOSC	2.93	3500-8900
SN2016jft	20170106	2457761.33	+12.7	YFOSC	2.93	3500-8900
SN2016jft	20170119	2457773.23	+24.6	YFOSC	2.93	3500-8900
SN2016jft	20170213	2457798.34	+49.7	YFOSC	2.93	3500-8900
SN2016jfu	20161231	2457754.38	+7.5	BFOSC	2.97	3700-8800
SN2016jfu	20170102	2457756.38	+9.6	BFOSC	2.97	3700-8800
SN2016jfu	20170104	2457758.35	+11.5	BFOSC	6.63	3700-8800
SN2016jfu	20170120	2457774.28	+27.5	BFOSC	11.8	3800-8800
SN2016jfu	20170131	2457785.35	+38.5	BFOSC	2.97	3800-8800
SN2016jfu	20170212	2457797.24	+50.4	YFOSC	2.93	3500-8900
SN2016N	20160118	2457406.08	+9.8	BFOSC	18.2	4200-8800
SN2017aub	20170217	2457802.11	+8.7	BFOSC	2.97	4000-8800
SN2017aub	20170222	2457807.03	+13.6	BFOSC	2.97	4000-8800
SN2017aub	20170225	2457809.95	+16.6	BFOSC	6.63	3700-8800
SN2017aub	20170303	2457815.95	+22.6	BFOSC	2.97	3700-8800
SN2017aub	20170308	2457820.97	+27.6	BFOSC	2.97	3700-8800
SN2017aub	20170317	2457829.99	+36.6	BFOSC	2.97	3700-8800
SN2017aub	20170328	2457840.98	+47.6	BFOSC	2.97	3700-8800
SN2017auf	20170217	2457802.06	+5.4	BFOSC	2.97	4000-8800
SN2017auu	20170216	2457801.01	+21.0	YFOSC	7.91	4000-8100
SN2017cfa	20170317	2457830.06	+8.4	BFOSC	2.97	4000-8800
SN2017cff	20170319	2457832.24	+12.0	YFOSC	2.93	3500-8900
SN2017cff	20170408	2457852.23	+32.0	YFOSC	2.93	3500-9200
SN2017cjb	20170328	2457841.22	+5.9	YFOSC	2.93	3500-8700
SN2017dka	20170502	2457876.31	+8.3	YFOSC	7.91	4000-8300
SN2017gtd	20170920	2458017.31	+8.3	BFOSC	2.97	3700-8800
SN2017gww	20170927	2458024.21	+1.1	BFOSC	2.97	3700-8800
SN2017gww	20171001	2458028.15	+5.1	YFOSC	2.93	3500-8900
SN2017gww	20171230	2458117.99	+94.9	YFOSC	2.93	3500-8900
SN2017hk	20170120	2457774.37	+16.2	YFOSC	2.93	3500-8900
SN2017hk	20170206	2457791.41	+33.2	YFOSC	2.93	3500-8900
SN2017hxx	20171112	2458070.20	+15.7	YFOSC	2.93	3500-8800
SN2017hxx	20171114	2458072.19	+17.7	YFOSC	2.93	3500-8800
SN2017hxx	20171120	2458078.07	+23.6	YFOSC	2.93	3500-8800
SN2017hxx	20171115	2458073.22	>19.3	YFOSC	2.93	3500-8800
SN2017imr	20171128	2458086.18	+19.1	YFOSC	2.93	3500-8900
SN2017iub	20171210	2458098.26	+8.8	BFOSC	2.97	4600-7100
SN2017ivu	20180212	2458162.27	+85.0	BFOSC	8.8	4000-8800
SN2017ivu	20180220	2458170.39	+93.2	YFOSC	2.93	3500-9000
SN2017ivu	20180301	2458179.42	+102.2	YFOSC	2.93	3500-9000
SN2017ivu	20180313	2458191.35	+114.1	YFOSC	2.93	3500-9000
SN2017jbj	20171230	2458118.02	>17.4	YFOSC	2.93	3500-8900
SN2018afm	20180323	2458200.97	+12.7	BFOSC	2.97	4000-8800
SN2018aoq	20180408	2458217.20	+8.7	BFOSC	2.97	4000-8800
SN2018aoq	20180410	2458219.12	+10.6	BFOSC	2.97	4000-8800
SN2018aoq	20180420	2458229.04	+20.5	OMR	9.6	3500-8800
SN2018aoq	20180424	2458233.13	+24.6	BFOSC	2.97	4000-8800
SN2018aoq	20180426	2458235.22	+26.7	BFOSC	2.97	4000-8800
SN2018aoq	20180428	2458237.13	+28.6	BFOSC	2.97	4000-8800
SN2018aoq	20180507	2458246.13	+37.6	BFOSC	2.97	4000-8800
SN2018aoq	20180604	2458274.11	+65.6	BFOSC	2.97	4000-8800
SN2018aoq	20180612	2458282.05	+73.5	BFOSC	2.97	4000-8800
SN2018aoq	20180623	2458293.04	+84.5	BFOSC	2.97	4000-8800
SN2018aql	20180514	2458253.20	+55.1	YFOSC	2.93	3500-9000
SN2018aql	20180515	2458254.32	+56.2	YFOSC	2.93	3500-9000
SN2018bek	20180506	2458245.27	+6.4	BFOSC	2.97	4000-8800
SN2018bek	20180507	2458246.17	+7.3	BFOSC	2.97	4000-8800
SN2018bek	20180508	2458247.22	+8.3	BFOSC	2.97	4000-8800
SN2018bek	20180517	2458256.07	+17.2	BFOSC	2.97	4000-8800
SN2018bek	20180523	2458262.23	+23.3	BFOSC	2.97	4000-8800
SN2018bek	20180602	2458272.09	+33.2	BFOSC	2.97	4000-8800
SN2018bek	20180604	2458274.22	+35.3	BFOSC	2.97	4000-8800
SN2018gk	20180123	2458142.35	+11.7	BFOSC	2.97	4000-8800
SN2018gk	20180212	2458162.32	+31.7	BFOSC	2.97	4000-8800
SN2018gk	20180222	2458172.33	+41.7	BFOSC	2.97	4000-8800
SN2018kpo	20181226	2458479.21	+2.9	YFOSC	2.93	4000-8800
SN2018lab	20181229	2458482.23	+1.1	YFOSC	2.93	3500-8800
SN2018lab	20181230	2458483.19	+2.1	YFOSC	2.93	3500-8800
SN2018lcd	20190104	2458487.99	+6.7	BFOSC	2.97	4000-8700

Line velocities and pseudo equivalent widths of H α , H β and Fe II 5169. (continue)

SN	phase	$v_{H\alpha}(\sigma)$	$v_{H\beta}(\sigma)$	$v_{FeII5169}(\sigma)$	$pew_{obs}^{H\alpha}(\sigma)$	$ pew_{emi}^{H\alpha}(\sigma) $	$pew_{obs}^{H\beta}(\sigma)$	$pew_{obs}^{FeII5169}(\sigma)$
SN2016hjh	>30.2	9123(589)	8118(1006)	5945(864)	28.06(0.01)	112.54(0.44)	38.76(0.24)	16.28(0.17)
SN2016hvu	>11.6	...	9044(708)	17.42(0.05)	...
SN2016hvu	>17.4	10820(708)	8854(285)	...	9.65(0.19)	279.34(5.54)	11.85(0.02)	...
SN2016hvu	>26.4	8176(267)	7452(571)	5235(400)	33.64(0.50)	224.92(1.51)	38.28(0.02)	14.77(0.07)
SN2016f	+21.1	8504(252)	7747(295)	6145(707)	16.91(0.07)	162.18(0.16)	41.57(0.62)	22.47(0.08)
SN2016jby	+45.6	7042(385)	5946(590)	4656(413)	21.19(0.06)	123.93(0.18)	36.65(0.03)	23.1(0.26)
SN2016jft	+12.7	...	9320(906)	9.7(0.15)	...
SN2016jft	+24.6	9122(421)	8461(501)	6450(619)	8.44(0.55)	127.81(0.16)	31.45(0.15)	18.18(0.08)
SN2016jft	+49.7	7795(414)	6231(1417)	4344(705)	29.55(0.19)	178.35(0.03)	54.24(0.88)	32.65(1.33)
SN2016jfu	+11.5	10835(627)	7909(333)	...	10.34(0.01)	37.90(0.03)	9.14(0.33)	...
SN2016jfu	+27.5	8100(513)	...	7043(226)	17.49(0.54)	173.19(3.06)	...	44.65(1.41)
SN2016jfu	+38.5	7063(480)	5662.6(810)	5494(1077)	33.57(0.11)	159.13(0.77)	32.15(0.84)	29.34(0.33)
SN2016jfu	+50.4	7203(509)	5493.9(1077)	3798(757)	41.56(0.15)	127.64(0.91)	28.86(0.19)	31.47(2.26)
SN2017aub	+8.7	...	8323(285)	9.35(1.04)	...
SN2017aub	+13.6	...	10329(380)	6260(269)	18.3(2.24)	40.61(2.11)
SN2017aub	+16.6	...	6509(702)	28.61(0.05)	...
SN2017aub	+22.6	6174(332)	4848(330)	4474(601)	9.01(0.26)	129.14(1.95)	16.98(0.70)	18.7(0.34)
SN2017aub	+36.6	5394(984)	4508(652)	3531(613)	30.71(0.08)	135.71(0.48)	15.76(1.21)	25.77(0.12)
SN2017aub	+47.6	4920(320)	4008(544)	2673(526)	41.9(0.63)	112.56(0.25)	40.7(0.84)	43.39(1.57)
SN2017auu	+21.0	10243(1187)	112.56(0.15)	21.87(0.33)
SN2017eff	+12.0	...	9218(513)	33.59(0.15)	...
SN2017eff	+32.0	7374(451)	6875(434)	4128(476)	29.12(0.08)	205.63(0.29)	45.09(0.03)	18.05(0.08)
SN2017cjb	+5.9	10837(389)	10453(488)	...	15.36(0.22)	78.86(0.07)	21.34(0.07)	...
SN2017gtd	+8.3	...	8492(286)	12.15(0.70)	...
SN2017hk	+16.2	...	10526(1077)	10.6(0.26)	...
SN2017hk	+33.2	9000(1090)	8876(1618)	7519(266)	13.94(0.47)	133.92(2.24)	45.02(2.93)	32.63(2.29)
SN2017hxx	+15.7	...	9630(1554)	22.11(0.80)	...
SN2017hxx	+17.7	...	9252(1168)	22.78(1.24)	...
SN2017hxx	+23.6	10721(395)	7449(947)	7477(857)	11.77(0.19)	114.34(0.86)	21.94(0.91)	16.8(1.29)
SN2017imr	+19.1	...	11681(1485)	22.43(4.02)	...
SN2017iub	+8.8	12296(451)	33.25(1.28)	177.70(0.01)
SN2017ivu	+85.0	7376(492)	6054(448)	3949(585)	71.68(0.14)	204.36(0.20)	54.52(0.15)	65.25(1.97)
SN2017ivu	+93.2	6789(329)	5874(592)	3775(641)	59.28(0.36)	139.00(0.31)	30.63(0.33)	52.67(3.07)
SN2017ivu	+102.2	6743(376)	5869(650)	3603(346)	65.82(0.06)	155.37(0.29)	35.02(0.71)	58.17(1.90)
SN2017ivu	+114.1	6347(386)	4929(395)	3511(424)	63.56(0.15)	173.46(1.00)	36.96(0.00)	57.91(0.03)
SN2017jbj	>+17.4	11381(219)	10704(838)	...	3.96(0.21)	157.08(1.10)	37.42(0.60)	...
SN2018afm	+12.7	...	9728.3(979.4)	15.54(1.00)	...
SN2018aoq	+8.7	8118.2(481.6)	7240.2(437.6)	...	4.8(0.02)	136.52(0.43)	25.8(0.44)	...
SN2018aoq	+10.6	7639.5(216.5)	6606.6(292.3)	...	7.17(0.01)	178.28(0.34)	26.97(0.60)	...
SN2018aoq	+20.5	6113.3(670.3)	5668.5(557.4)	4262.8(359.0)	25.27(0.21)	186.04(0.16)	64.18(0.86)	28.68(0.91)
SN2018aoq	+24.6	6778.3(281.1)	5260.3(292.3)	4152.4(274.9)	35.63(0.02)	185.54(0.15)	43.41(0.46)	20.21(0.07)
SN2018aoq	+26.7	6530.2(286.8)	4777.5(291.7)	3575.5(274.3)	42.66(0.15)	168.85(0.21)	44.8(1.29)	17.6(0.14)
SN2018aoq	+28.6	5576.1(435.6)	3992.5(388.0)	3387(364.9)	44.15(0.71)	157.64(0.74)	37.2(0.81)	29.52(1.58)
SN2018aoq	+37.6	5434.2(340.5)	3600.7(292.2)	2921.7(274.8)	57.76(0.02)	136.95(0.36)	51.57(0.18)	28.42(0.13)
SN2018aoq	+65.6	4454.5(216.3)	...	1928.3(274.6)	65.28(0.78)	88.72(0.17)	30.16(0.07)	44.29(0.05)
SN2018aoq	+73.5	4480.8(273.8)	...	1875.7(347.7)	64.21(0.26)	80.97(0.06)	15.19(1.66)	40.32(1.33)
SN2018aoq	+84.5	4237.2(216.5)	...	1563.5(274.9)	58.98(0.17)	70.52(0.01)	20.11(1.49)	44.62(0.58)
SN2018aql	+56.2	3007.9(217.2)	14.54(0.04)
SN2018bek	+17.2	...	9769.9(599.5)	14.02(0.88)	...
SN2018bek	+23.3	6471(599.5)	6633.9(1401.8)	...	2.98(0.30)	60.86(0.66)	10.99(0.13)	...
SN2018bek	+33.2	6408.1(945.3)	4749.5(331)	3951.5(678.5)	0.25(0.04)	94.20(1.47)	26.09(1.48)	12.02(0.11)
SN2018gk	+31.7	11102.4(442.6)	8926.9(589.2)	...	6.88(0.23)	112.05(0.04)	24.75(0.11)	...
SN2018gk	+41.7	11101.7(757.6)	9923.3(1464.4)	6451(943.7)	14.41(0.07)	181.46(0.04)	50.8(0.24)	11.36(0.10)
SN2018pn	+18.9	5795.6(212)	4217.1(544.9)	3520.9(357.5)	30.78(0.05)	229.42(0.01)	30.07(0.01)	23.99(0.40)
SN2018rz	+25.1	10263.7(653.9)	8525.9(1324.3)	7602.1(268.9)	17.82(3.52)	161.81(0.19)	44.84(0.22)	17.45(0.13)
SN2018yo	+39.7	11293.1(218.4)	7806.7(514.9)	5214.8(277.4)	102.73(0.02)	206.57(1.50)	66.58(0.01)	35.45(0.84)

The unit of velocities is km s⁻¹ and the unit of pew is Å

Table A4. Velocity at 50 days after explosion and power-law exponent of our sample and well-studied sample in literature.

name	$v_{\text{H}\alpha}^{50}(\sigma)$ km s ⁻¹	$n_{\text{H}\alpha}(\sigma)$	$v_{\text{H}\beta}^{50}(\sigma)$ km s ⁻¹	$n_{\text{H}\beta}(\sigma)$	$v_{\text{Fe}}^{50}(\sigma)$ km s ⁻¹	$n_{\text{Fe}}(\sigma)$
PS15cwo	8850(203)	-0.218(0.069)	7798(269)	-0.153(0.049)	5185(644)	-0.264(0.345)
SN2011az	3356(1373)	-0.861(0.403)
SN2011bi	8396(385)	-0.201(0.138)	6922(812)	-0.513(0.271)	5439(449)	-0.255(0.214)
SN2011fu	7118(1555)	-0.176(0.145)
SN2012A	5649(137)	-0.267(0.048)	4558(236)	-0.433(0.081)	2813(229)	-0.608(0.128)
SN2012fs	4251(489)	-0.629(0.097)
SN2013ab	6606(377)	-0.255(0.037)	4205(479)	-0.481(0.064)
SN2013gd	6649(589)	-0.263(0.143)	3144(944)	-1.066(0.438)	3638(246)	-0.539(0.145)
SN2014G	8008(203)	-0.157(0.051)	6755(385)	-0.337(0.094)	4935(387)	-0.606(0.130)
SN2014cx	7888(268)	-0.315(0.037)	6288(440)	-0.413(0.076)	4242(457)	-0.552(0.206)
SN2014cy	4955(320)	-0.208(0.095)	3659(357)	-0.436(0.132)	2502(371)	-0.685(0.179)
SN2014dq	5593(282)	-0.227(0.037)	4264(336)	-0.359(0.071)	2629(402)	-0.587(0.395)
SN2015V	6481(276)	-0.265(0.289)	5031(405)	-0.343(0.063)	3352(348)	-1.019(0.624)
SN2015cz	5988(264)	-0.395(0.083)	5885(891)	-0.339(0.157)	3044(397)	-0.677(0.202)
SN2016B	6721(799)	-0.387(0.148)
SN2016hvu	6997(435)	-0.267(0.056)	6733(912)	-0.240(0.126)
SN2016jft	7784(417)	-0.224(0.100)	7063(889)	-0.223(0.137)	4329(708)	-0.562(0.268)
SN2016jfu	6822(339)	-0.307(0.057)	5368(699)	-0.264(0.094)	3843(668)	-1.013(0.297)
SN2017aub	4871(301)	-0.293(0.077)	4141(292)	-0.448(0.049)	2713(379)	-0.642(0.116)
SN2017cff	6016(573)	-0.299(0.086)
SN2017hk	8052(2352)	-0.238(0.291)
SN2017hxu	4537(2038)	-0.668(0.462)
SN2017ivu	9116(1772)	-0.440(0.285)	8784(2110)	-0.671(0.355)	4850(2135)	-0.403(0.623)
SN2018aoq	5036(103)	-0.284(0.019)	3559(193)	-0.411(0.045)	2358(133)	-0.708(0.088)
SN2018bek	3022(360)	-1.097(0.142)
SN1999em	5657(307)	-0.327(0.034)	4158(321)	-0.504(0.102)	3369(59)	-0.587(0.018)
SN2003gd	3567(27)	-0.514(0.008)
SN2004dj	5593(61)	-0.472(0.041)	3360(27)	-0.514(0.031)
SN2004et	6895(34)	-0.255(0.013)	5844(101)	-0.379(0.018)	4096(29)	-0.592(0.017)
SN2005cs	1812(346)	-0.755(0.282)
SN2008bk	2067(23)	-0.403(0.022)
SN2009N	4908(104)	-0.436(0.049)	3028(49)	-0.829(0.027)	2356(87)	-0.840(0.066)
SN2012aw	7004(186)	-0.327(0.020)	5144(252)	-0.413(0.035)	4203(93)	-0.566(0.025)
SN2012ec	6813(117)	-0.372(0.017)	4910(529)	-0.522(0.106)	3755(33)	-0.640(0.017)
SN2013ej	7615(102)	-0.198(0.011)	6133(192)	-0.299(0.024)	4380(196)	-0.611(0.056)
SN2013fs	8010(264)	-0.204(0.041)	6812(192)	-0.29(0.033)	4109(62)	-0.557(0.028)
SN2015bf	5209(476)	-0.350(0.148)	4081(173)	-0.532(0.067)
SN2016bkv	1576(93)	-0.290(0.108)	1354(77)	-0.400(0.083)	1328(76)	-0.303(0.087)
SN2017eaw	7421(157)	-0.297(0.157)	5578(197)	-0.499(0.02)	4741(56)	-0.567(0.021)
SN2018zd	4346(69)	-0.310(0.063)	3554(40)	-0.593(0.004)	3215(34)	-0.377(0.041)

This paper has been typeset from a \TeX/L\AA\TeX file prepared by the author.

Table A6. pEW of H α at 50 days after explosion

SN	H $\alpha_{\text{obs}}^{50}(\sigma)$	H $\alpha_{\text{emi}}^{50}(\sigma)$	H $\alpha_{\text{o/e}}^{50}$
PS15cwo	32.87(0.16)	-219.65(0.40)	0.14
SN2011bi	41.41(2.07)	-186.57(0.53)	0.24
SN2012ec	58.93(1.71)	-157.90(1.29)	0.38
SN2013gd	24.57(0.01)	-114.51(0.07)	0.35
SN2014G	21.87(1.22)	-205.86(0.34)	0.11
SN2014cx	72.57(0.21)	-183.46(0.68)	0.40
SN2014cy	31.01(0.07)	-82.63(0.02)	0.38
SN2014dq	52.89(0.23)	-184.36(0.21)	0.29
SN2015V	67.15(0.54)	-185.65(0.74)	0.37
SN2015cz	32.61(0.02)	-137.40(1.15)	0.24
SN2016jft	29.55(0.19)	-178.35(0.03)	0.17
SN2016jfu	41.56(0.15)	-127.64(0.91)	0.33
SN2017aub	41.90(0.63)	-112.56(0.25)	0.37
SN2018aoq	61.09(0.78)	-115.59(0.40)	0.56
SN2012fc	54.95(0.25)	-327.85(0.67)	0.17
SN2013af	97.99(0.04)	-178.25(0.39)	0.55
SN2014A	57.56(0.29)	-96.20(0.12)	0.60
SN2014B	44.88(1.14)	-224.62(0.24)	0.20
SN2015W	47.55(0.13)	-226.44(0.76)	0.21
SN2016aip	60.60(1.76)	-200.19(2.16)	0.30
SN2016jby	21.19(0.06)	-123.93(0.18)	0.17
SN2012A	44.87 (0.13)	-204.44(0.38)	0.22